JCI insight

EZH2 deletion does not impact acinar regeneration but restricts progression to pancreatic cancer in mice

Emilie Jaune-Pons, … , Gwen Lomberk, Christopher L. Pin

JCI Insight. 2024. https://doi.org/10.1172/jci.insight.173746.

Research In-Press Preview Oncology

Graphical abstract

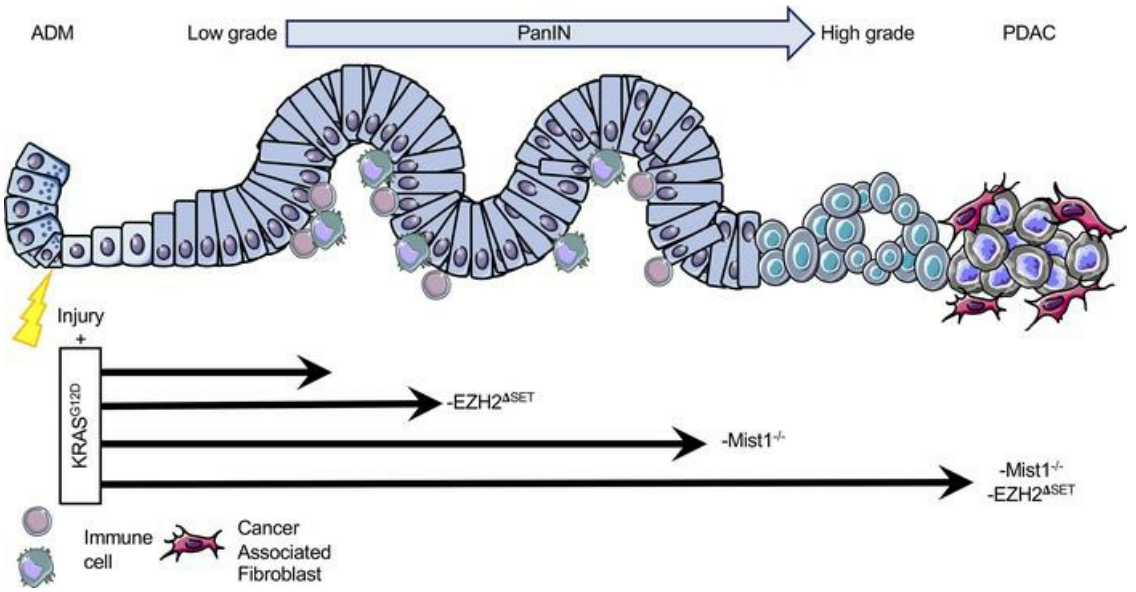

EZH2 deletion does not impact acinar regeneration but restricts progression to pancreatic cancer in mice

Emilie Jaune-Pons[1,4,5*], Xiaoyi Wang[1,4,5*], Fatemeh Mousavi[1,4,5*], Zachary Klassen[1,4,5], Samad Elkaoutari[7], Kurt Berger[2,4], Charis Johnson[3,5], Mickenzie B. Martin[1,4,5], Saloni Aggarwal[5], Sukhman Brar[5], Khalid Muhammad[5], Joanna Ryan[1,5], Parisa Shooshtari[2,5], Angela J. Mathison[6,7], Nelson Dusetti[9], Raul Urrutia[6,7], Gwen Lomberk[6,7,8], and Christopher L. Pin[1,3-5]

Affiliations

Departments of [1]Physiology and Pharmacology, [2]Pathology and Laboratory Medicine, [3]Paediatrics, and [4]Oncology, Schulich School of Medicine and Dentistry, Western University, London, Ontario, Canada; [5]Verspeeten Family Cancer Centre, London, Ontario, Canada, [6]Department of Surgery, Division of Research, Medical College of Wisconsin, Milwaukee, WI, USA, [7]Linda T. and John A. Mellowes Center for Genomic Sciences and Precision Medicine, Medical College of Wisconsin, Milwaukee, WI [8]Department of Pharmacology and Toxicology, Medical College of Wisconsin, Milwaukee, WI [9]Centre de Recherche en Cancérologie de Marseille (CRCM), Unité 1068, Institut National de la Santé et de la Recherche Médicale, Marseille, France

Correspondence:

Dr Christopher L. Pin,

A4-913, Cancer Research Laboratory Program

Victoria Campus, London Health Sciences Centre

800 Commissioners Road E

London, ON, N6C 2V5

Telephone: 519-685-8500 x53073

Fax: 519-685-8616

Email: cpin@uwo.ca

*Shared first authorship

Conflict-of-interest statement:

The authors have declared that no conflict of interest exists.

Abstract:

Enhancer of Zeste Homologue 2 (EZH2) is part of the Polycomb Repressor Complex 2, which promotes trimethylation of lysine 27 on histone 3 (H3K27me3) and genes repression. EZH2 is overexpressed in many cancers and studies in mice attributed both pro-oncogenic and tumor suppressive functions to EZH2 in pancreatic ductal adenocarcinoma (PDAC). EZH2 deletion enhances *de novo* KRAS-driven neoplasia following pancreatic injury, while increased EZH2 expression in PDAC patients is correlated to poor prognosis, suggesting a context-dependant effect for EZH2 in PDAC progression. In this study, we examined EZH2 in pre- and early neoplastic stages of PDAC. Using an inducible model to delete the SET domain of EZH2 in adult acinar cells ($EZH2^{\Delta SET}$), we showed loss of EZH2 activity did not prevent acinar cell regeneration in the absence of oncogenic KRAS ($KRAS^{G12D}$), nor increase PanIN formation following $KRAS^{G12D}$ activation in adult mice. Loss of EZH2 did reduce recruitment of inflammatory cells and, when combined with a more aggressive PDAC model, promoted widespread PDAC progression and remodeling of the tumor microenvironment. This study suggests expression of EZH2 in adult acinar cells restricts PDAC initiation and progression by affecting both the tumour microenvironment and acinar cell differentiation.

Introduction:

Pancreatic ductal adenocarcinoma (PDAC) is the most common form of pancreatic cancer with the worst five-year survival, ~12%, of any of the major cancers (Pancreatic Cancer Facts, PANCAN). The principle driver mutation in PDAC is activating *KRAS* mutations, which occurs in >90 % of PDAC patients (1). Oncogenic KRAS mutations, such as $KRAS^{G12D}$, appear at early stages of the disease but are not enough to induce PDAC on their own (2, 3). Several studies indicate environmental stressors, in addition to somatic mutations in *KRAS*, are required for PDAC progression. Chronic inflammation is associated with increased sensitivity to $KRAS^{G12D}$, indicating environmental factors contribute to progression (4). Based on these findings, there is increasing interest in the role epigenetic mediators have in initiation and progression of PDAC. Mutations in several genes encoding epigenetic modifiers, including *ARID1A* and *KMT2D* (5), are found in PDAC patients, and activation of $KRAS^{G12D}$ is associated with extensive changes in the epigenetic profile of cells (6). In addition, Enhancer of Zeste Homolog 2 (EZH2) is highly expressed in a subset of PDAC tumours and correlated to poor prognosis (7).

EZH2 is a histone-lysine N-methyltransferase enzyme and part of the Polycomb Repressive Complex 2 (PRC2), which plays a critical role in cell fate specification during embryonic development (8, 9). EZH2 induces trimethylation of H3K27me3 (K27me3), a histone modification linked to chromatin remodeling and gene repression (10). EZH2 is overexpressed in many cancers (7, 11), but both pro-oncogenic and tumor suppressive roles have be reported in the context of PDAC (12, 13). In the developing pancreas, EZH2 establishes long term gene expression profiles, and deletion of the SET domain, which is responsible for methyltransferase activity, reduces acinar cell regeneration after injury and increases pancreatic intraepithelial neoplasia (PanIN) initiation and tumor progression (12). Using a similar mouse model, loss of EZH2 methyltransferase activity

during development along with expressing $KRAS^{G12D}$ initially favoured PanIN progression, but reduced PanIN maintenance in aged mice compare to $KRAS^{G12D}$ alone (14). This study proposed a role for EZH2 in NFATc1 regulation and PDAC progression, suggesting the EZH2's role may extend to the tumour microenvironment (14). More recent studies show *EZH2* deletion in pancreatic cancer cells increased GATA6 expression, a marker of classical PDAC subtype, indicating the presence of EZH2 promotes a more aggressive, basal-like PDAC subtype (13). Coupled with the findings that increased EZH2 expression correlates to more advanced disease and increased therapeutic resistance (15, 16), it appears EZH2's role differs between early stages of PDAC initiation and later progression and resistance.

In this study, we examined EZH2 function in pre-neoplastic stages of PDAC, focusing on EZH2's impact on acinar cell regeneration and PanIN initiation in adult mice. Since PDAC patients present later in life (>60 years of age), we used a pre-clinical model which allows $KRAS^{G12D}$ induction in adult acinar cells of the pancreas, instead of embryonic induction of $KRAS^{G12D}$ (12, 14). We employed a similar approach to alter EZH2 function, in which the SET domain of EZH2 ($EZH2^{\Delta SET}$) is deleted, but used an inducible cre recombinase that promoted deletion in only acinar cells of the adult pancreas. Unlike previous studies, our results indicate loss of EZH2 activity has minimal impact on acinar cell regeneration and does not enhance PanIN initiation, but initially favours more advanced PanIN lesion development in the context of $KRAS^{G12D}$. Loss of EZH2 SET activity in combination with $KRAS^{G12D}$ induces reprogramming of the genome based on H3K27me3 enrichment and reduces immune cell recruitment in response to injury. Conversely, deleting $EZH2^{\Delta SET}$ in a susceptible mouse model for PDAC ($Mist1^{creERT/-}KRAS^{G12D}$) greatly enhanced PanIN progression and PDAC formation. This study highlights several, context dependent roles for EZH2 in PDAC initiation and progression. EZH2 helps mediate $KRAS^{G12D}$-

induced reprogramming of the acinar cell genome, primes immune and inflammatory genes in these cells which allows for a differential immune response, and is required for long term expansion of pre-neoplastic lesions.

Results:

KRAS^{G12D} promotes widespread epigenetic remodeling in acinar cells

To examine the epigenetic response to oncogenic KRAS, KRAS^{G12D} expression was induced in acinar cells of 2-4-month-old *Mist1*$^{creERT/+}$*KRAS*^{G12D} mice (referred as *KRAS*^{G12D}) by tamoxifen (TX) gavage (**Figure S1A**). Twenty-two days after KRAS^{G12D} activation, H&E histology showed no differences in acinar cell morphology (**Figure 1A**). ChIP-seq for H3K27me3 (K27me3) and H3K4me3 (K4me3) was performed on whole pancreatic tissue as these marks are linked to gene repression and activation and can maintain genes in a primed state (17). Such priming has been identified in pancreatic development and adult tissue (18–20), and involves enrichment K4me3and K27me3 at the same genomic regions (21, 22).

The total number of K4me3-enriched regions decreased slightly (~1.1%) in *KRAS*^{G12D} tissue, while the number of sites enriched for K27me3 was substantially higher (~38.5%) in *KRAS*^{G12D} pancreata (n=3 mice/genotype; **Table 1**). The distribution of K4me3 and K27me3 enrichment within the genome was similar between genotypes (**Figure S1B**) and heatmaps confirmed little change in K4me3 enrichment around genes (**Figure 1B**). Heat maps for K27me3 suggested some uniquely enriched TSSs in *KRAS*^{G12D} and control pancreata (boxed areas, **Figure 1B**). Comparing TSSs between genotypes supported a general increase in K27me3 enrichment in *KRAS*^{G12D} pancreata (**Figure 1C**) while changes in K4me3-enriched TSSs, which were more numerous, were uniformly distributed between the two genotypes (**Figure 1C**).

To determine regions of gene priming in the acinar genome, we classified chromatin states based on K27me3 and K4me3 marks. We defined four distinct states - state 1 is absent for both marks, state 2 (K27me3) and state 3 (K4me3) contain single marks, and state 4, the primed state, contains both (**Figure 1D**). Distribution of states 2 to 4 did not change (**Figure S1C**) between genotypes, with most state 2 regions located distally from genes and states 3 and 4 closely associated with gene bodies. Correlation to transcriptomic data obtained from the same pancreatic samples confirmed state 4 enrichment at CpG islands is associated with reduced expression compared to genes in state 3, and resembled expression of genes associated with state 2 (**Figure 1E**). *KRAS^{G12D}* tissue showed a marked increase in state 4 enriched CpG islands relative to control tissue, which are associated with enhancer regions and gene regulation (**Figure 1D**). These findings suggest KRAS^{G12D} expression promotes increased K27me3 enrichment in acinar cells, and can affect epigenetically primed regions within the genome.

EZH2 methyltransferase restricts KRAS^{G12D}-mediated PanIN progression following injury.

Since K27me3 involves EZH2 (23, 24), we examined the effects of deleting EZH2 methyltransferase activity in the context of KRAS^{G12D}. A similar model to previous studies was used, with loxP sites flanking *Ezh2* exons 16 to 19, which encompasses the SET domain (12, 25). We employed a *Mist1* cre-driver that allows inducible and acinar-specific *Ezh2* deletion and KRAS^{G12D} activation in adult acinar cells (**Figure S2A**). To induce PanIN formation, activation of KRAS^{G12D} expression was combined with a two-day cerulein regimen, 15 and 17 days after initial KRAS^{G12D} activation (**Figure S2B;** (26)). PanIN progression was compared 35 days after initial cerulein treatment in *KRAS^{G12D}* and *Mist1$^{creERT/+}$KRAS$^{LSL\text{-}G12D}$Ezh2$^{\Delta SET/\Delta SET}$* (referred to as *KRAS^{G12D}Ezh2$^{\Delta SET}$*) mice. C57Bl6 mice, or mice carrying only the *Mist1^{creERT}* allele, were used as

controls since loss of a single *Mist1* allele has no effect on gene expression (both indicated as control). We also included mice carrying the *Mist1*^{creERT} allele and homozygous for the *Ezh2*$^{\Delta SET}$ allele (*Mist1*$^{creERT/+}$*Ezh2*$^{\Delta SET}$, called *EZH2*$^{\Delta SET}$). No group showed overt differences based on final weights regardless of whether mice were treated with cerulein or saline (**Figure S2C**). Similarly, pancreatic weight as a percentage of body weight showed no differences at the time of dissection (**Figure S2D**).

Histological analysis of control and *EZH2*$^{\Delta SET}$ pancreatic tissue showed no differences in pancreatic morphology (**Figure S2E**), different from previous studies which suggested EZH2 was required for acinar cell regeneration (12). Since this study used a longer, recurrent model of CIP (cerulein-induced-pancreatitis), the response of *Ezh2*$^{\Delta SET}$ mice to twice daily injections of 250 μg/kg cerulein over two weeks was examined (**Figure S3A**; (27)). As previously reported, increased EZH2 accumulation was observed in response to injury in tissue from control animals, with EZH2 completely absent in *Ezh2*$^{\Delta SET}$ tissue (**Figure S3B**). However, recurrent injury still showed no differences in body (**Figure S3C**) or pancreas to body weight (**Figure S3D**), pancreatic morphology (**Figure S3E**), or amylase accumulation (**Figures S3B, F**) between genotypes. Both control and *EZH2*$^{\Delta SET}$ pancreatic tissue had increased CK19 accumulation following CIP (**Figure S3G**) with no difference in accumulation between genotypes. This suggests acinar cell regeneration is not restricted upon EZH2$^{\Delta SET}$ deletion in mature acinar cells. Thus, we returned to the acute-CIP model to assess the impact of *Ezh2*$^{\Delta SET}$ deletion on KRAS^{G12D}-mediated PanIN progression.

Five weeks after KRAS^{G12D} activation, saline-treated *KRAS*^{G12D} and *KRAS*^{G12D}*Ezh2*$^{\Delta SET}$ pancreatic tissue showed sporadic lesions (<1% of the entire tissue area). Cerulein treatment resulted in intralobular lesions containing ADM and PanINs in *KRAS*^{G12D} expressing tissue. While *KRAS*^{G12D}

mice had more lesions (29 ± 11.5%) than *KRAS^{G12D}Ezh2$^{\Delta SET}$* (13.7 ± 3.2%) mice, the difference was not significant (**Figure 2A**, **S4A**). To quantify ADM and PanINs, we compared the ratio of CK19 (marker of ADM and PanINs) to amylase accumulation (**Figure 2B**). While a trend towards increased CK19 accumulation in *KRAS^{G12D}Ezh2$^{\Delta SET}$* mice was observed, it was not significant compared to *KRAS^{G12D}* mice (p=0.219). However, measures of PanIN progression, including Alcian Blue (**Figures 2C,** lower magnification **S4B**) and PAS (Periodic Acid Schiff) histology (**Figure 2D,** lower magnification **S4C**), showed *KRAS^{G12D}Ezh2$^{\Delta SET}$* mice had significantly more staining of PanINs compared to *KRAS^{G12D}* mice. suggesting EZH2 limited progression to more advanced PanIN lesions.

Next, K27me3 enrichment was assessed in *KRAS^{G12D}Ezh2$^{\Delta SET}$* tissue 22 days after KRAS^{G12D} activation and prior to injury induction, and integrated with earlier analysis of *KRAS^{G12D}* and control pancreatic tissue (**Table 1**). At this time point, pancreatic tissue retained normal histology in all genotypes (**Figures 1A, S5A**). The number of K27me3 enrichment sites was higher (8.3% increase) in *KRAS^{G12D}Ezh2$^{\Delta SET}$* vs. control tissues, but markedly lower (27.8% decrease) compared to *KRAS^{G12D}* tissue, confirming the absence of EZH2 methyltransferase activity reduced the ability of KRAS^{G12D} to reprogram the genome (**Table 1**). Analysis of K4me3 identified modest increases in the number of enriched sites in *KRAS^{G12D}Ezh2$^{\Delta SET}$* tissue compared to both control (+3.2%), and *KRAS^{G12D}* tissue (+4.3%; **Table 1**).

To call genes targeted for reprogramming, enrichment peaks associated with gene bodies were identified. K27me3 enrichment typically occurs as BLOCs that extend over 100 kb (28). Therefore, we called genes based on K27me3 sites between -100 kb and +3 kb from TSSs. This criterion identified substantially more K27me3-annotated genes in *KRAS^{G12D}* over control tissue (+31.6%,

Table 1). Conversely, *KRAS^{G12D}Ezh2$^{\Delta SET}$* tissue showed only a 9.8% increase in K27me3-enriched genes compared to control tissue, with 16.6% fewer K27me3-annotated genes than *KRAS^{G12D}* tissue (**Table 1, Figure S5B**). Of the 1,515 genes enriched for K27me3 in *KRAS^{G12D}* but not control tissue, less than half (692; 45.7%) were also enriched in *KRAS^{G12D}Ezh2$^{\Delta SET}$* tissue **(Figure S5C**). Alternatively, K4me3 peaks are located close to TSSs, typically 1-4 kb in breadth (28) and we used a range of +/- 3 kb from TSSs to call genes. The number of K4me3-enriched genes in control tissue was very similar to both *KRAS^{G12D}* (+0.7%) and *KRAS^{G12D}Ezh2$^{\Delta SET}$* tissues (-0.4%), suggesting loss of EZH2 methyltransferase activity does not affect enrichment of this mark (**Table 1**).

We next assessed the effects of KRAS^{G12D} on acinar cell gene expression at the same 22-day time point. RNA-seq analysis identified 380 differentially expressed genes (DEGs; **Figure 3A, Appendix 1**) between control and KRAS^{G12D} tissue, markedly fewer changes when compared to changes in K27me3 enrichment. Interesting, combined loss of EZH2 methyltransferase activity with *KRAS^{G12D}* had a more profound effect on gene expression than *KRAS^{G12D}* alone. *KRAS^{G12D}Ezh2$^{\Delta SET}$* pancreatic tissue had 811 DEGs compared to control (**Figure 3B, Appendix 1**) and 315 DEGs compared to *KRAS^{G12D}* tissue (**Figure 3C, Appendix 1**). To determine if changes in gene expression was related to epigenetic reprogramming, we integrated RNA-seq data with the ChIP-seq data. State 2 and 4 genes were examined as they represent targets of EZH2. For the great majority of state 2 genes uniquely enriched for K27me3 in each genotype, no corresponding changes in gene expression were observed (>97%; **Figure S6A**), consistent with previous observations (29). Changes in gene expression rarely corresponded to uniquely-called state 4 peaks within a genotype (**Table 1**), indicating most epigenetic changes correlating to *KRAS^{G12D}* activity were silent. 2.8% of state 4 genes unique to control tissue are differentially expressed between control and either *KRAS^{G12D}* or *KRAS^{G12D}Ezh2$^{\Delta SET}$* tissue (**Table 1)**. Similarly, 1.7% of *KRAS^{G12D}*

and 4.3% of *KRAS^{G12D}Ezh2$^{\Delta SET}$* State 4 genes are also DEGs. Alignment with RNA-seq data showed state 4 genes in *KRAS^{G12D}Ezh2$^{\Delta SET}$* have lower expression patterns similar to state 2 genes (**Figure 1E**) but, consistent with a role for EZH2 in KRAS^{G12D}-mediated silencing, higher expression of state 2 and 4 genes was observed in *KRAS^{G12D}Ezh2$^{\Delta SET}$* tissue compared to control and *KRAS^{G12D}* tissue (**Figure 1E**).

Alterations in state 4 genes suggests priming may lead to different responses to environmental cues. KEGG analysis of state 4 enriched genes showed *KRAS^{G12D}* tissue had many more uniquely enriched pathways compared to control or *KRAS^{G12D}Ezh2$^{\Delta SET}$* tissue including RAS and PI3K/Akt signaling (**Figure 3D, Table S1**). While more pathways were enriched in *KRAS^{G12D}* tissue, KEGG analysis using state 2 genes showed no difference in KEGG pathways between genotypes (**Figure S6B, Table S2**). Similar KEGG pathway analysis of DEGs between *KRAS^{G12D}* or *KRAS^{G12D}Ezh2$^{\Delta SET}$* tissue and control tissue showed enrichment for MAPK signaling in both genotypes, but only *KRAS^{G12D}Ezh2$^{\Delta SET}$* tissue was enriched for P13K/Akt signaling (**Figure 3E, Table S3**) and Gene Set Enrichment Analysis shows enhanced activation of KRAS-UP signaling (**Figure 3F**) and P13K/AKT signaling (**Figure S6C**) in *KRAS^{G12D}Ezh2$^{\Delta SET}$* tissue compared to both control and *KRAS^{G12D}* tissues. This supports a mechanism in which EZH2 restricts activation of KRAS-mediated pathways and may account for the more progressive PanINs observed in *KRAS^{G12D}Ezh2$^{\Delta SET}$* tissue.

Direct comparison of *KRAS^{G12D}* and *KRAS^{G12D}Ezh2$^{\Delta SET}$* transcriptomics also identified immune-related pathways as differentially enriched (**Figure 4A, Table S4**). While previous studies suggested KRAS works through EZH2 and NFATc1 to affect an inflammatory response (30), RNA-seq analysis showed no differences in *Nfatc1* expression between genotypes (**Figure S7A**)

and immune cell infiltration based on $CD3^+$ (T lymphocytes), $CD4^+$ (helper T cells), $CD8^+$ (cytotoxic T cells) and $F4/80^+$ (macrophages) expression was not observed in either $KRAS^{G12D}$ and $KRAS^{G12D}Ezh2^{\Delta SET}$ tissue without cerulein treatment (**Figure S7B**). However, several DEGs in the immune-related pathways, including *Cd1d1* (**Figure 4B**), *Colec12*, *Maf*, *H2-Q6*, and *H2-Q7* (**Figure S7C**), showed K27me3 enrichment peaks in $KRAS^{G12D}$ but not $KRAS^{G12D}Ezh2^{\Delta SET}$ tissue.

Examination five-weeks after acute cerulein injury showed accumulation of $CD3^+$, $CD4^+$, $CD8^+$ and $F4/80^+$ cells surrounding PanIN lesions in $KRAS^{G12D}$ tissue (**Figures 4C, D**). While $KRAS^{G12D}Ezh2^{\Delta SET}$ tissue had similar accumulation of $CD3^+$ and $CD4^+$ cells, a significant reduction in $F4/80^+$ cells ($p<0.001$) and a trend towards decreased $CD8^+$ cells ($p=0.095$) was observed (**Figure 4C**). Similar analysis for vimentin and α-SMA, markers of cancer-associated fibroblasts, showed no difference between $KRAS^{G12D}$ and $KRAS^{G12D}Ezh2^{\Delta SET}$ mice (**Figure 4E**). Combined, this data suggests an EZH2-dependent mechanism in which $KRAS^{G12D}$ reprograms the acinar cell epigenome, and effects infiltration of immune cells upon injury.

Loss of EZH2 activity promotes rapid progression of PDAC in $Mist1^{creERT/-}KRAS^{G12D}$ model.

Our findings on EZH2's role in early PanIN progression differed from previous studies. One possibility is EZH2's role differs depending on the susceptibility of the model to $KRAS^{G12D}$. Therefore we assessed whether EZH2 showed a similar ability to restrict PanIN progression in a more severe model of PDAC. We generated $Mist1^{creERT/creERT}KRAS^{G12D}$ mice with (indicated as $Mist1^{creERT/-}KRAS^{G12D}$) and without the EZH2 ΔSET domain ($Mist1^{creERT/-}KRAS^{G12D}Ezh2^{\Delta SET}$; indicated as *MKE*; **Figure S8A**) as loss of MIST1 markedly increases sensitivity to $KRAS^{G12D}$ (31). Gross morphological analysis 2 months after $KRAS^{G12D}$ activation (**Figure S8B**) revealed no differences in weight between control, $KRAS^{G12D}$, $KRAS^{G12D}Ezh2^{\Delta SET}$, $Mist1^{creERT/-}KRAS^{G12D}$ and

MKE cohorts (**Figure S8C**). However, three *MKE* mice needed to be sacrificed prior to the experimental end point. In addition, mice expressing $KRAS^{G12D}$ often developed oral mucosa tumours (data not shown), likely due to $Mist1^{creERT}$ activity in this tissue, forcing us to cease the experiment at 60 days after initial TX treatment. While most genotypes showed relatively normal pancreatic tissue, $Mist1^{creERT/-}KRAS^{G12D}$ pancreata contained some fibrotic masses (**Figure S8D**; blue arrows) not observed in $KRAS^{G12D}$ and $KRAS^{G12D}Ezh2^{\Delta SET}$, consistent with the development of preneoplastic nodules. Pancreatic nodule formation dramatically increased in the absence of EZH2 in $Mist1^{creERT/-}KRAS^{G12D}$ mice (*MKE*).

Increased EZH2 accumulation was confirmed in $Mist1^{creERT/-}KRAS^{G12D}$ pancreatic tissue at the mRNA **(Figure 5A)** and protein level **(Figure 5B)** and was lower in *MKE* mice. RNA-seq showing *Ezh2* tracks confirmed deletion of exon 16 to 19 (**Figure 5C**) and amylase protein (**Figure 5B**) and mRNA (**Figure 5D**) were decreased in *MKE* tissue, suggesting negligible acinar tissue in these mice. Conversely, ERK levels were elevated in $Mist1^{creERT/-}KRAS^{G12D}$ and MKE extracts (**Figure 5B**). H&E staining (**Figure 5E**) and IHC for amylase (**Figure 6A, B**) confirmed minimal acinar tissue and development of high grade PanINs and PDAC in *MKE* mice (**Figure 5E-G**). *MKE* pancreata also exhibited widespread fibrosis and invasive PDAC while $Mist1^{creERT/-}KRAS^{G12D}$ mice showed some progression to more advanced PanINs (**Figure 5E**). $KRAS^{G12D}$ and $KRAS^{G12D}Ezh2^{\Delta SET}$ mice showed few lesions, consisting of ADM and low grade PanINs. Extensive PanIN lesions in *MKE* mice was confirmed by IHC for CK19 (**Figure 6C**), and IF (**Figures 6D, E**) and RNA-seq (**Figure S9A**) for SOX9, a marker of neoplastic lesions, supported markedly increased $KRAS^{G12D}$-mediated PanIN progression to PDAC.

We next integrated RNA-seq data from *Mist1*$^{creERT/-}$*KRAS*^{G12D} and *MKE* tissue with the earlier transcriptomic analysis (**Figure 3**). 22 days after KRAS^{G12D} activation, no lesions were observed in any genotype except *MKE* tissue, which showed focal ADM (**Figure 7A, S9B**). As expected, *MKE* mice clustered separately from all other genotypes based on transcriptomic analysis (**Figure 7B**). *Mist1*$^{creERT/-}$*KRAS*^{G12D} and *MKE* tissue had 7,636 DEGs (**Appendix 2**; **Figure 7C**), including many ncRNAs. Gene Set Enrichment Analysis (GSEA) using the 6,255 protein-encoding DEGs identified >150 significantly altered pathways (**Table S5**) including nucleosome and chromatin remodelling suggesting substantial effects on the acinar cell genome in *MKE* tissue (**Figure 7D, E**). Highly enriched pathways in *MKE* mice were also related to TME remodeling and an increased inflammatory response (**Figure 7E**). *Ptgs2*, which encodes the pro-inflammatory protein COX2 (**Figure S9C**), was markedly increased only in *MKE* tissue. While negligible fibrosis was evident at the time of transcriptomic analysis (**Figure S9B**), trichrome blue histology showed extensive fibrosis 60 days after treatment in *MKE* pancreata (**Figure 7F**).

These findings reveal EZH2's effect on acinar cell transformation but contributions from the ECM and inflammatory responses may contribute to PanIN progression. Therefore, to examine ADM in the absence of the microenvironment, acinar cells were isolated 22 days after activation of KRAS^{G12D} and cultured in a 3D collagen matrix (**Figure 8A**). EZH2 recombination was almost complete at this time point, (**Figure 5A**) and transcriptome analysis confirmed no compensation by *Ezh1* and *Kdm6a/b* occurs in *Ezh2*-deleted cultures (**Figure S10A**). ADM was assessed for 9 days following isolation (**Figure 8B, C**). All genotypes showed increased ADM relative to control cultures, with the number of viable ADM decreasing after day 5 except for *Mist1*$^{creERT/-}$*KRAS*^{G12D} and *MKE* cultures (**Figure 8C**). *Mist1*$^{creERT/-}$*KRAS*^{G12D} cultures showed little difference in size from controls, but ADMs were maintained until the end of culture. *MKE* acini developed more rapidly

into ADM with ~100% conversion by day 3 and continued to increase in size throughout the culture, showing no obvious apoptosis or necrosis. Staining for Ki67 identified proliferating cells only in *MKE* and *KRAS^{G12D}EZH2$^{\Delta SET}$* ADM, consistent with previous reports of EZH2-mediated regulation of cell cycle genes (**Figure S10B**; (12, 32, 33). *p16/CDKN2A*, which affects both senescent and cell cycle pathways, was elevated in *MKE* mice (**Figure 10C**), consistent with EZH2's role in repressing its expression. Interesting, *p16/CDKN2A* was not altered in *KRAS^{G12D}EZH2$^{\Delta SET}$* tissue. Additionally, acinar cultures derived from control mice treated with increasing concentrations of the EZH2 inhibitor, EPZ6438, also showed an increase in ADM at 6 days (**Figure 8D, E**), consistent with EZH2 restricting initial ADM.

To determine if the absence of EZH2 effects the maintenance of epithelial neoplasias, we developed 3D organoid cultures from *KRAS^{G12D}*, *KRAS^{G12D}Ezh2$^{\Delta SET}$* and *MKE* pancreatic tissue two weeks after cerulein induction (**Figure S11A, B**) when PanINs have developed (**Figure 9A**). Organoids were readily observed in *KRAS^{G12D}* cultures but *KRAS^{G12D}Ezh2$^{\Delta SET}$* cultures showed few, smaller organoids (**Figure 9B**), a difference maintained upon passaging (**Figure 9C**). While organoids from *MKE* tissue initially appeared similar to cultures developed from *KRAS^{G12D}* tissue **(Figure 9B)**, after only one passage, *MKE* organoids showed rapid growth and larger organoid structures compared to *KRAS^{G12D}* or *KRAS^{G12D}Ezh2$^{\Delta SET}$* cultures (**Figure 9C, D**). To show an ongoing requirement for EZH2 in neoplastic cells, *Mist1$^{creERT/-}$KRAS^{G12D}* organoids were developed from CIP-treated mice and exposed to EPZ6438 for 7 days and growth compared to *MKE* organoids. At the time of dissection, *Mist1$^{creERT/-}$KRAS^{G12D}* tissue showed extensive ADM, but maintained the lobular nature of the pancreas and did not show the same extent of fibrosis as that observed in *MKE* tissue (**Figure S11C**) EZH2 inhibition markedly increased the size of *Mist1$^{creERT/-}$KRAS^{G12D}* organoids becoming similar in size to *MKE* organoids (**Figure S11D-F**).

These 3D cultures highlight that cell autonomous events are, at least partially, responsible for the *MKE* phenotype and increased progression to PDAC observed in *MKE* mice and support a contextual role for EZH2 in early PDAC progression.

Discussion:

In this study, the impact of $KRAS^{G12D}$ and loss of EZH2 on epigenetic remodeling, neoplastic lesion development, and progression was examined. Using a model allowing inducible activation of $KRAS^{G12D}$ in acinar cells of adult mice, we showed $KRAS^{G12D}$ promotes epigenetic reprogramming of the acinar cell genome, leading to widespread EZH2-dependent H3K27me3 enrichment. EZH2 is dispensable for acinar cell regeneration following pancreatic injury but restricts PanIN progression following acute injury combined with $KRAS^{G12D}$. While this difference did not result in high-grade PanIN lesions, loss of $EZH2^{\Delta SET}$ activity greatly enhanced PDAC progression in mice $Mist1^{creERT/-}KRAS^{G12D}$, leading to spontaneous loss of acinar tissue, substantial fibrosis, and PDAC within 60 days. This is the first study that examines changes in acinar cell K27me3 enrichment profiles directly related to $KRAS^{G12D}$ expression, how these changes are affected by EZH2 function, and shows context-specific roles for EZH2 that promote or restrict early PanIN progression. This study also highlights the importance of epigenetic reprogramming in the context of PDAC and suggests EZH2 restricts early PanIN progression to PDAC through priming of immune and inflammatory genes.

$KRAS^{G12D}$ promotes epigenetic repression of the acinar cell genome

Our findings support a model in which KRAS^{G12D} promotes general epigenetic repression within the pancreas prior to overt morphological changes. Global enrichment of K27me3 was increased in *KRAS^{G12D}* compared to control tissue, while global K4me3 enrichment was similar between KRAS^{G12D} +/- tissue. This is consistent with studies showing increased expression and activity of DNA methyltransferases, histone deacetylases, and PRC1 and 2 in PDAC (34–37), all of which promote epigenetic repression. Importantly, epigenetic reprogramming does not accompany widespread transcriptomic dysregulation, suggesting changes in the epigenome predate transcriptional differences and may be masked until additional environmental stresses are present. We previously characterized similar epigenetic reprogramming of acinar cells in response to chronic stress which suggested reprogramming alters the molecular response to subsequent acute stimuli (38). One mechanism that underlies reprogramming involved changes to "primed" genes, which have bivalent epigenetic enrichment for active and repressive epigenetic marks. This epigenetic bivalency allows repressed genes to be rapidly activated and involves K27me3 enrichment. The widespread enrichment of K27me3 following KRAS^{G12D} activation suggests EZH2, in part, regulates reprogramming. In support of these findings, deletion of EZH2 in the presence of KRAS^{G12D} resulted in K27me3 enrichment levels comparable to control tissue.

Loss of EZH2 leads to epigenetic reprogramming of pathways involved inflammation

While EZH2 has been targeted in several other studies examining its role in PDAC (15, 39, 40), this is the first study that examines global K27me3 enrichment in the context of EZH2 loss of function. K27me3 ChIP-Seq combined with RNA-Seq revealed increased enrichment of immune-related pathways 22 days after KRAS^{G12D} induction that appears to prime the genome for a differential inflammatory response since no immune cell infiltration was observed in the pancreas until after induction of injury. Two and five weeks after pancreatic injury, *KRAS^{G12D}* mice showed

an increase immune cell infiltration such as $CD3^+$, $CD4^+$, $CD8^+$ lymphocytes and $F4/80^+$ macrophages cells. The accumulation of each of these cell types was reduced in the absence of $EZH2^{\Delta SET}$ activity, suggesting loss of EZH2 activity in $KRAS^{G12D}Ezh2^{\Delta SET}$ mice drives an immune cold environment. Decreased accumulation of $CD4^+$ and $CD8^+$ cells would promote PDAC progression as their presence is associated with improved prognosis of PDAC patients (41–43). These findings support recent studies that propose a direct role for EZH2 in immune cell recruitment and activation in cancer (44, 45) and suggest EZH2 plays a protective role in early PanIN development by increasing specific $CD45^+$ immune cell infiltration such as $CD4^+$ and $CD8^+$ cell recruitment. However, the absence of EZH2 activity also results in decreased accumulation of $F4/80^+$ macrophages cells, which are generally associated with enhanced PDAC progression since these favor immunosuppressive environment (46, 47). The contradiction supports a more complex involvement of EZH2 that is likely stage dependent. This is supported by analysis of organoids developed from $KRAS^{G12D}Ezh2^{\Delta SET}$ and $KRAS^{G12D}$ pancreatic tissue, which showed no difference in vivo, but exhibited marked differences *ex vivo*. Organoids developed from $KRAS^{G12D}Ezh2^{\Delta SET}$ tissue had reduced size and number suggesting Ezh2-negative lesions have a reduced ability for long term progression. The different outcomes between *in vivo* and *ex vivo* following altered *Ezh2* function could suggest a non-cell intrinsic role for EZH2 in affecting the tissue microenvironment, and this is supported by the differences in immune cell infiltrate. However, it is also possible that early advantages gained by the loss of EZH2 in promoting PanIN differentiation are lost as PanINs progress to a more advanced phenotype. This phenomenon is consistent with observations in Chen et al (14), which showed the increased PanIN progression initially observed in the absence of EZH2 was not maintained at later stages. However, the disadvantage of not having EZH2 as PanINs

progress appears to be bypassed by the loss of MIST1. Whether this is still due to external differences within the microenvironment will need to be assessed.

Loss of EZH2$^{\Delta SET}$ activity enhances a susceptible environment for KRAS^{G12D}-mediated PDAC

As mentioned, while our findings suggest a protective role for EZH2 in limiting early PanIN progression, previous studies on EZH2 show a more critical role in early stages of PDAC. Using the same floxed *EZH2$^{\Delta SET}$* allele, Mallen-St Clair et al (12) showed acinar cell regeneration was restricted following cerulein-induced injury and increased KRAS^{G12D}-mediated PanIN initiation and progression, consistent with a restrictive role for EZH2 methyltransferase function (12, 14). As mentioned above, Chen et al (14) supported these findings but suggested EZH2 was necessary for maintaining pre-neoplastic lesions, with fewer PanIN lesions apparent in older mice. Our results revealed negligible effects on acinar cell regeneration as *KRAS^{G12D}* and *KRAS^{G12D}Ezh2$^{\Delta SET}$* mice developed similar numbers of PanINs lesions following injury. We suggest the discrepancy in our results arises, in part, from the *cre* driver used in the two studies having different effects on susceptibility to KRAS^{G12D}. Previous studies achieved *Ezh2$^{\Delta SET}$* deletion by targeting a non-inducible *cre* recombinase to the *Ptf1a* or *Pdx1* genes resulting in *KRAS^{G12D}* activation in early pancreatic development, prior to differentiation of mature pancreatic cell types. EZH2 is important for early development and specification (8) of acinar and liver cells from a common endodermal origin. In the absence of EZH2, epigenetic programs that fix in the differentiation status of mature cell types are absent. *Mist1^{creERT}* mice allow *Ezh2$^{\Delta SET}$* deletion and *KRAS^{G12D}* activation only in mature acinar cells when mature epigenetic programs are already in place. Therefore, epigenetic programs that establish an adult phenotype are not affected. In addition, haploinsufficiency for *Ptf1A* likely affects the response to KRAS^{G12D}. Loss of a single *Ptf1a* allele alters the cell fate of

acinar cells (48) which increases the potential for undergoing ADM. Conversely, loss of a single *Mist1* allele shows no differences in acinar cell function, response to injury or gene expression when compared to wild type litter mates. Only when MIST1 is completely absent do acinar cells show incomplete differentiation and increased sensitivity to injury and $KRAS^{G12D}$ (31, 49). In support of the importance of the cre driver for studying PanIN progression, comparison of $Ptf1a^{creERT/+}KRAS^{G12D}$ mice to $Mist1^{creERT/+}KRAS^{G12D}$ or $Elastase^{creERT/+}KRAS^{G12D}$ mice showed marked differences in sensitivity to cerulein-induced injury (Mousavi et al, in revision).

Loss of EZH2 methyltransferase activity leads to both cell autonomous and non-cell autonomous effects on PDAC progression

Despite the differences, both the current study and Chen et al (14) confirm a protective role for EZH2 in restricting early PanIN progression and PDAC development. We suggest this effect of EZH2 is through both cell autonomous and non-cell autonomous effects within the pancreas. RNA sequencing at 22 days revealed loss of EZH2 activity in $Mist1^{creERT/-}KRAS^{G12D}$ mice (i.e. *MKE*) leads to activation of pathways involved in TME remodeling that favour aggressive PDAC progression (50–52) and the rapid progression to ADM and PanINs appears to be independent of the TME. RNA-seq analysis also revealed loss of EZH2 had a substantial impact on pathways affecting chromatin stability in *MKE* acini suggesting a cell autonomous role for EZH2 in acinar cell reprogramming. This role was confirmed by culturing acinar cells of all genotypes in collagen 22 days after tamoxifen-induced recombination or culturing organoids from $KRAS^{G12D}$ and MKE genotypes following acute cerulein treatment. In collagen cultures, *MKE* acini showed rapid ADM compared to other genotypes, with increased proliferation, and maintained survival over the length of culture. In matrigel cultures, *MKE* organoids show rapid growth and formed and maintained larger cyst structures compared to the $KRAS^{G12D}$ cultures. Interestingly, inhibition of EZH2 both in

control acinar cells and *Mist1*$^{creERT/-}$*KRAS*^{G12D} organoids induces and increase of ADM formation and organoids size, respectively.

Targeting EZH2 function has been suggested as a possible therapy based on in vitro and xenograft data showing EZH2 inhibitors can enhance sensitivity to traditional chemotherapy (53). While our results support and extend findings of the importance of EZH2 in restricting progression to PDAC, they do not agree with studies on PDAC cell lines or tissue obtained from patients. Increased EZH2 expression in PDAC is correlated to worse prognosis and resistance to therapy (13, 15, 39). Crucially, these previous studies suggest the effects of EZH2 are independent of its methyltransferase activity. Therefore, it is likely EZH2 has additional, non-PRC2 functions relevant to late stage PDAC, which our study does not addressed. However, our findings suggest targeting EZH2 in PDAC with pharmacological inhibitors must be approached with caution.

While this is the first study to identify specific EZH2 roles on epigenetic reprogramming following induction of KRAS^{G12D}, there are limitations to the work. H3K4 and H3K27 are only two epigenetic modifications linked to gene expression, and other modifications are more consistent with gene expression. K36me3 and K9me3 enrichment are more closely correlated with gene expression and repression, respectively, and DNA methylation is highly correlated to gene repression. While we have focused on K4me3 and K27me3 due to their roles in epigenetic bivalency, a more comprehensive analysis is warranted. Similarly, while *Mist1-creERT* driver mice provide a more relevant model of PDAC compared to previous studies using *Ptf1a-cre* mice, which activates KRAS^{G12D} in development, an inducible *Ptf1a-creERT* model is available that would allow longer term analysis given its pancreas-specific expression. However, this model shows

increased sensitivity to $KRAS^{G12D}$ that may not be physiologically relevant (Mousavi et al, in revision).

To conclude, our study shows EZH2 limits progression from acinar cells to late stage PDAC through reprogramming of inflammatory and extracellular matrix genes. These effects are likely through both non-cell autonomous and cell autonomous mechanisms. Loss of EZH2 alters pathways that promote inflammation and fibrosis, thereby affecting the TME, but also enhances ADM in the absence of the TME. This work highlights a complex role for EZH2 in initiating and progression of pancreatic cancer. While our findings support a tumour suppressive role in restricting PanIN and PDAC formation, future studies are needed to determine if these effects are simply due to PRC2-related functions or additional modes of EZH2 activity.

Materials and Methods:

Sex as a biological variable

In this study, both male and female C57Bl6 mice were used for each genotype. Sex was not considered as a biological variable in this study.

Mouse models

Our study examined male and female animals, and similar findings are reported for both sexes. In all experiments, both male and female mice were used to reach significance. Mice were given normal chow and water ad libitum throughout the experiment. C57/Bl6 mice containing *loxP* sites flanking exons 16 to 19 of the *Ezh2* gene (encompass the SET domain; $Ezh2^{\Delta SET/\Delta SET}$), an oncogenic $KRAS^{G12D}$ within the *Kras* locus and downstream of a *loxP-stop-loxP* (*LSL*) cassette ($Kras^{LSL\text{-}G12D}$), or an inducible cre recombinase (creERT) targeted to the *Mist1* coding region ($Mist1^{creERT}$), have been used and described previously (12, 18, 25, 54, 55). Mating of these transgenic lines lead to eight distinct genotypes which were confirmed before and after experimentation using the primers indicated in **Table S6**. To induce *loxP* recombination, two to four-month-old mice were gavaged 3 times over 5 days with 2 mg tamoxifen (TX; Sigma #T5648) in corn oil (Sigma #C8267). This regime has been used previously to induce >95% recombination in acinar cells of the $Mist1^{creERT}$ line (31, 56). Mice were sacrificed either 22 days or 60 days after the initial TX gavage or treated with cerulein to induce acute or recurrent pancreatic injury (see below). Pancreatic tissue was weighed and processed for paraffin sectioning, RNA, chromatin, or protein isolation.

Cerulein-induced pancreatitis

To induce acute pancreatic injury, 2-4-month-old mice received eight hourly intraperitoneal injections of cerulein (50 mg/kg, MedChemExpress, #FI-6934) 15 and 17 days after the first dose of TX. Control mice received 0.9% saline solution. Mice were weighed every day to monitor weight changes and health, then sacrificed 14 or 35 days after initiating acute CIP.

To induce recurrent pancreatic injury, mice received intraperitoneal injections of cerulein (250 μg/kg body weight) or 0.9% saline solution (control) twice daily (9:00 h and 15:00 h) for 14 days. Mice were weighed daily to determine changes in body weight. Mice were sacrificed 7 days after the last cerulein injections.

RNA isolation, RNA-seq and data analysis

RNA was isolated from whole pancreatic tissue of mice 22 days after TX induction using Trizol (Invitrogen, #15596018) followed by the Pure link kit following manufacturer's instructions (Invitrogen, #12183018A). RNA was prepared for RNA-seq as previously described (33). Two (for *Mist1*$^{creERT/-}$*KRAS*^{G12D}) or three (*Control*, *EZH2*$^{\Delta SET}$, *KRAS*^{G12D}, *KRAS*^{G12D}*EZH2*$^{\Delta SET}$, and *MKE*) biological replicates per group were sequenced using the Illumina NextSeq High Output 150 cycle (paired-end sequencing) sequencing kits. The complete RNA-seq data can be found at GEO accession GSE (GSE262920 and GSE252884). RNA-seq reads were aligned to mouse genome mm10 and sorted by coordinate using STAR v2.7.9a (57). Gene counts were generated using the featureCounts function of the Subread v2.0.3 aligner (58) and the subsequent differential expression analysis performed using the edgeR v3.321 package (59, 60). The differentially expressed genes acquired from this analysis were used in subsequent functional analysis and later in the comparison to genes obtained from ChIP-seq analysis. Functional and enrichment analysis,

including KEGG and Gene Ontology (GO) pathway analyses and Gene Set Enrichment, were performed using clusterProfiler v3.18.1 R package (61). A threshold of p-adjusted ≤ 0.05 cut off was used for all differential expression and pathway analyses. PCA plots v2.2.0 (DOI: 10.18129/B9.bioc.PCAtools), Venn diagrams v1.7.3 (62), and dotplots v1.10.2 (63) were generated using the corresponding R package.

ChIP-Sequencing and data analysis

Chromatin was isolated from pancreatic tissue of mice 22 days after TX gavage. The ChIP-seq protocol was followed as previously described (38). Antibodies against K27me3 (Millipore Sigma #07-449) or K4me3 (Millipore Sigma #04-745) were used for immunoprecipitation and subsequent next-generation sequencing was performed using Illumina NextSeq High Output 150 cycle sequencing kit. The complete ChIP-seq data can be found at GEO accession GSE (GSE262919). Raw data were first checked for read quality using FastQC and aligner against the mouse genome (mm10) using bowtie2 tool (64). Identification of the peaks for each sample was performed using Homer FindPeaks tool with the "histone" mode, which searches for broad regions of enrichment of variable width by comparing both local background and corresponding input samples. Genomic annotation and visualization of the peaks was performed using ChIPSeeker R package and *TxDb.Mmusculus.UCSC.mm10.knownGene* library. To define the target genes with marked ChIP enrichment, we defined the promoter region of +/- 3 kb from the TSS (transcription start site). Genes overlapping at least one identified peak were considered target genes for a given sample. KEGG enrichment analysis was performed based on the resulting lists of target genes using ClusterProfiler R package. Heatmap visualization of the ChIP enrichment was performed using ngs.plot tool (65) with decreasing ranking of genes based on the ChIP enrichment level among the gene body. Bed files with H3K4me3 and H3K27me3 aligned reads and their corresponding input

samples were used to assess chromatin states with ChromHMM (66). The resulting output generated 4 chromatin states. The enrichment of each state was calculated and visualized and the states were annotated based on the enrichment patterns.

Real-time qRT-PCR analysis

Real time qRT-PCR was performed on cDNA samples prepared as described (38). Expression of *Ptgs2* were normalized to mitochondrial ribosomal protein L1 (*Mrpl1*). ViiA 7 RUO software (Applied Biosystems) was used to calculate the amount of RNA relative to wild type animals for the equivalent time points. Primer sequences are shown in **Table S7**.

Tissue fixation and histology

For histological analysis, pancreatic tissue was isolated from the head and tail of the pancreas and processed as described (38). To assess overall histology and identify differences in pancreatic tissue architecture, sections were stained with H&E. Lesions area were quantified using ImageJ as percent of total tissue area. Mucin accumulation was visualized using an Alcian Blue stain kit (Abcam, #ab150662) and staining quantified as a percentage of the whole tissue area. Periodic-acid Schiff staining was also performed (Sigma-Aldrich Kit; #3951 and 3952) and quantified by scoring PanIN lesions as PAS+ (>50%), partially PAS+ (<50%), or PAS negative. To assess fibrosis, paraffin sections were stained using Trichrome Blue (Abcam, #ab150686). Lesions and other staining were scored over at least three sections from both the duodenal and splenic regions of the pancreas.

Immunohistochemistry and immunofluorescence

IHC was performed on paraffin sections as described (38). Following antigen retrieval, sections were permeabilized with 0.2% Triton-X (BDH, #R06433) in PBS, rinsed, then blocked in 5% sheep serum in PBS for 1 hour at room temperature. Primary antibodies were diluted in 5% sheep serum in PBS and incubated overnight at 4°C. Primary antibodies included rabbit amylase (Cell signaling Technology, #4017, 1:400), rabbit CK19 (Abcam, #15463, 1:200), rabbit CD3 (BD Biosciences, #560591, 1:200), rabbit CD8 (Thermofisher, #98941, 1:200), rabbit F4/80 (Abcam, #ab111101, 1:100), rabbit α-SMA (Cell signaling technology, #19245, 1:200), rabbit Vimentin (Cell signaling technology, #5741, 1:400). Sections were washed, then incubated in biotinylated mouse α-rabbit IgG secondary antibody (in 5% sheep serum, Vector, #PK-4001, 1:1000) for 30 min at room temperature. Finally, sections were incubated in AB reagent for 30 min at room temperature and visualized using ImmPACT DAB Peroxidase (HRP) substrate (Vector, #PK-4001/SK-4105). Slides were counterstained with hematoxylin (Biocare Medical, #CATHE-M) and imaged using Leica Microscope DM5500B (Leica Microsystems) and LAS V4.4 software.

IF analysis was performed on paraffin-embedded tissue sections for SOX9, CD4 and for KI67, acinar cells were fixed in PFA 3% and then embedded in paraffin. Slides were prepared as for IHC except for quenching with hydrogen peroxidase (Fisher Scientific, #H325) for SOX9. Primary antibody is rabbit SOX9 (Millipore Sigma, #AB5535, 1:250), rat CD4 (Thermofisher, #14-0041-82, 1:250) and mouse KI67 (BD Biosciences, #550609, 1:250). After washing, slides were incubated in α-rabbit or α-mouse IgG conjugated to TRITC (Jackson ImmunoResearch, #711-025-152 and #715-025-150, 1:300) diluted in 5% sheep serum in PBS. Prior to mounting in Vectashield Permafluor mountant (Thermo Fisher Scientific, #SP15), sections were incubated in DAPI (Thermo Fisher Scientific, #62248). Staining was visualized using Leica DFC365 FX camera on the Leica DM5500B microscope. Images were taken on Leica LASV4.4 software.

Protein isolation and Western blotting

Pancreatic protein was isolated as described (67) and quantified using a Bradford protein assay (Bio-Rad, #5000006). Isolated protein was resolved by SDS-PAGE and transferred to polyvinylidene fluoride membrane (Bio-Rad, #162-0177). Western blot analysis was carried out as described (68) using antibodies specific for rabbit EZH2 (Cell signaling technology, #5246, 1:1000), rabbit Amylase (Abcam, #ab21156, 1:8000), rabbit Total ERK (Cell signaling technology, #9102, 1:1000). After washing, blots were incubated in α-rabbit HRP antibody (Cell signaling technology, #7074, 1:3000). Blots were visualized using the VersaDoc Imaging System with Quantity One 1-D Analysis software (Bio-Rad).

Acinar cell isolation and 3D-Collagen culture

Acinar cells were isolated and embedded in collagen as previously described (69). Cyst formation was assessed every day until day 9 in culture. At day 7, some cultures were processed for paraffin sectioning and IF analysis for Ki67. Representative images were taken with an upright Leica microscope.

Organoid isolation and 3D-Matrigel culture

The middle section of the pancreas was isolated and digested based on previously published protocols with some modifications (70). Pancreata was digested by incubation in 1 mg/ml of collagenase/dispase for 20 minutes at 37°C in a rotating incubator. Digested tissue was washed with DMEM/F12 containing with 10 mM HEPES, 1% glutamax, 1% PenStrep and 100 µg/mL primocin and centrifuged at 300 g for 5 minutes. Supernatant was aspirated and tissue resuspended in StemPro Accutase (Gibco, cat #A11105-01) and incubated for 45 minutes at 37°C in a rotating

incubator. The resulting slurry was filtered through a 70 µm nylon mesh filter and cells resuspended in feeding media (71) with 5% Matrigel. 30 000 cells were seeded on a layer of 100% Matrigel (Corning, cat #356230). After first passage, organoids were reseeded into 100% Matrigel domes for experimental analysis according to (72). For passaging, organoids were incubated in 1 mg/ml of collagenase/dispase for 2 hours at 37°C, then rinsed with wash media and centrifuged at 300 g for 5 minutes. Supernatants were aspirated and cells resuspended in StemPro Accutase and incubated for 45 minutes at 37°C in a rotating incubator. Cells were centrifuged at 300 g for 5 minutes and supernatant aspirated. 5 000 cells were reseeded at equal densities in 100% Matrigel and supplemented with feeding media.

Statistical analysis

For ADM 3D-culture quantification, we used two-way repeated ANOVA followed by Dunnett's correction. For organoid quantification, we used a two-way ANOVA followed by Tukey's correction. For in vivo experiment, when two conditions were compared, a two-tailed unpaired Mann Whitney test was used. For more than two conditions comparison, one-way ANOVAs followed by Tukey's correction were performed. Pvalue or adjusted pvalue ≤ 0.05 were considered significant for all our analysis.

Study Approval

All experiments on mice were approved by the Animal Care Committee at the University of Western Ontario (Protocols #2020-057 and #2020-058).

Data availability

We have uploaded data to NCBI. The complete RNA-seq data can be found at GEO accession GSE (GSE262920 and GSE252884) and the complete ChIP-seq data can be found at GEO accession GSE (GSE262919).

Author contributions:

EJP – data acquisition and interpretation, manuscript writing and editing; XW – data acquisition and interpretation, manuscript writing; FM– data acquisition and interpretation, manuscript writing and editing; ZK – data acquisition; SE – data acquisition and interpretation; KB – data acquisition; CJ – data acquisition and interpretation; MBM – data acquisition; SA – data acquisition; SB – data acquisition; KM – data acquisition; JR – data acquisition; PS - data interpretation, mentorship; AJM - data acquisition and interpretation, manuscript editing; ND- data interpretation, mentorship; RU- data interpretation, mentorship; GL- data interpretation, mentorship; and CLP – study design, data interpretation, manuscript writing and editing, mentorship

Acknowledgments:

The authors wish to acknowledge the ongoing support of several national research funding agencies for this work including the Canadian Institutes of Health Research (MOP#PJT166029), the Cancer Research Society of Canada and the Rob Lutterman Foundation for Pancreatic Cancer Research. We are also indebted to support from the Baker Centre for Pancreatic Cancer. FM and EJP are supported by Mitacs Accelerate Fellowships.

Table 1A. Analysis of H3K27me3 and H3K27me3 enrichment in pancreatic tissue

Genotype	*Enriched Regions		Enriched Genes		Uniquely Enriched		Bivalent (DEGs**)	
	K27me3	K4me3	K27me3	K4me3	K27me3	K4me3	Total	Unique
Control	13164	21899	3555	11,698	4211	13163	1254	108 (3)
KRAS^{G12D}	18235	21667	4678	11,618	5298	13045	1652	299 (5)
KRAS^{G12D} *Ezh2*$^{\Delta SET}$	14251	22591	3903	11,650	4502	13160	1392	115 (5)

*n=3 mice/genotype, common peaks p_{adj}<0.05
** DEGs from RNA-seq analysis

Bibliography:

1. Hezel AF, et al. Genetics and biology of pancreatic ductal adenocarcinoma. *Genes Dev*. 2006;20(10):1218–1249.

2. De La O J-P, et al. Notch and Kras reprogram pancreatic acinar cells to ductal intraepithelial neoplasia. *Proc Natl Acad Sci U S A*. 2008;105(48):18907–18912.

3. Guerra C, et al. Chronic pancreatitis is essential for induction of pancreatic ductal adenocarcinoma by K-Ras oncogenes in adult mice. *Cancer Cell*. 2007;11(3):291–302.

4. Bansod S, Dodhiawala PB, Lim K-H. Oncogenic KRAS-Induced Feedback Inflammatory Signaling in Pancreatic Cancer: An Overview and New Therapeutic Opportunities. *Cancers (Basel)*. 2021;13(21):5481.

5. Wang SS, et al. Epigenetic Alterations in Pancreatic Cancer Metastasis. *Biomolecules*. 2021;11(8):1082.

6. Mathison AJ, et al. KrasG12D induces changes in chromatin territories that differentially impact early nuclear reprogramming in pancreatic cells. *Genome Biol*. 2021;22(1):289.

7. Gan L, et al. The polycomb group protein EZH2 induces epithelial-mesenchymal transition and pluripotent phenotype of gastric cancer cells by binding to PTEN promoter. *J Hematol Oncol*. 2018;11(1):9.

8. Huang X-J, et al. EZH2 is essential for development of mouse preimplantation embryos. *Reprod Fertil Dev*. 2014;26(8):1166–1175.

9. O'Carroll D, et al. The polycomb-group gene Ezh2 is required for early mouse development. *Mol Cell Biol*. 2001;21(13):4330–4336.

10. Margueron R, et al. Ezh1 and Ezh2 Maintain Repressive Chromatin through Different Mechanisms. *Molecular Cell*. 2008;32(4):503–518.

11. Bachmann IM, et al. EZH2 expression is associated with high proliferation rate and

aggressive tumor subgroups in cutaneous melanoma and cancers of the endometrium, prostate, and breast. *J Clin Oncol*. 2006;24(2):268–273.

12. Mallen-St Clair J, et al. EZH2 couples pancreatic regeneration to neoplastic progression. *Genes Dev*. 2012;26(5):439–444.

13. Patil S, et al. EZH2 Regulates Pancreatic Cancer Subtype Identity and Tumor Progression via Transcriptional Repression of GATA6. *Cancer Res*. 2020;80(21):4620–4632.

14. Chen N-M, et al. Context-Dependent Epigenetic Regulation of Nuclear Factor of Activated T Cells 1 in Pancreatic Plasticity. *Gastroenterology*. 2017;152(6):1507-1520.e15.

15. Ougolkov AV, Bilim VN, Billadeau DD. Regulation of pancreatic tumor cell proliferation and chemoresistance by the histone methyltransferase enhancer of zeste homologue 2. *Clin Cancer Res*. 2008;14(21):6790–6796.

16. Yuan S, et al. SOX8 Affects Tumoral SPARC Expression by Regulating EZH2 to Attenuate Effectiveness of albumin-bound paclitaxel in PDAC. *Int J Biol Sci*. 2022;18(3):911–922.

17. Grindheim JM, et al. Polycomb Repressive Complex 2 Proteins EZH1 and EZH2 Regulate Timing of Postnatal Hepatocyte Maturation and Fibrosis by Repressing Genes With Euchromatic Promoters in Mice. *Gastroenterology*. 2019;156(6):1834–1848.

18. Mehmood R, et al. Epigenetic reprogramming in Mist1(-/-) mice predicts the molecular response to cerulein-induced pancreatitis. *PLoS One*. 2014;9(1):e84182.

19. Falvo DJ, et al. *An epigenetic memory of inflammation controls context-dependent lineage plasticity in the pancreas*. Cancer Biology; 2021.

20. Wang A, et al. Epigenetic Priming of Enhancers Predicts Developmental Competence of hESC-Derived Endodermal Lineage Intermediates. *Cell Stem Cell*. 2015;16(4):386–399.

21. Xie R, et al. Dynamic Chromatin Remodeling Mediated by Polycomb Proteins Orchestrates Pancreatic Differentiation of Human Embryonic Stem Cells. *Cell Stem Cell*. 2013;12(2):224–

237.

22. Yu X-X, et al. Dynamics of chromatin marks and the role of JMJD3 during pancreatic endocrine cell fate commitment. *Development*. 2018;145(6):dev163162.

23. Pan M-R, et al. Orchestration of H3K27 methylation: mechanisms and therapeutic implication. *Cell Mol Life Sci*. 2018;75(2):209–223.

24. Simon JA, Lange CA. Roles of the EZH2 histone methyltransferase in cancer epigenetics. *Mutat Res*. 2008;647(1–2):21–29.

25. Su I-H, et al. Ezh2 controls B cell development through histone H3 methylation and Igh rearrangement. *Nat Immunol*. 2003;4(2):124–131.

26. Jeong YK, Kim H. A Mini-Review on the Effect of Docosahexaenoic Acid (DHA) on Cerulein-Induced and Hypertriglyceridemic Acute Pancreatitis. *Int J Mol Sci*. 2017;18(11):E2239.

27. Halbrook CJ, et al. Mitogen-activated Protein Kinase Kinase Activity Maintains Acinar-to-Ductal Metaplasia and Is Required for Organ Regeneration in Pancreatitis. *Cell Mol Gastroenterol Hepatol*. 2017;3(1):99–118.

28. Pauler FM, et al. H3K27me3 forms BLOCs over silent genes and intergenic regions and specifies a histone banding pattern on a mouse autosomal chromosome. *Genome Res*. 2009;19(2):221–233.

29. Pin CL, Ryan JF, Mehmood R. Acinar cell reprogramming: a clinically important target in pancreatic disease. *Epigenomics*. 2015;7(2):267–81.

30. Baumgart S, et al. Inflammation-induced NFATc1-STAT3 transcription complex promotes pancreatic cancer initiation by KrasG12D. *Cancer Discov*. 2014;4(6):688–701.

31. Shi G, et al. Loss of the acinar-restricted transcription factor Mist1 accelerates Kras-induced pancreatic intraepithelial neoplasia. *Gastroenterology*. 2009;136(4):1368–1378.

32. Yao Y, et al. Downregulation of Enhancer of Zeste Homolog 2 (EZH2) is essential for the Induction of Autophagy and Apoptosis in Colorectal Cancer Cells. *Genes (Basel)*. 2016;7(10):E83.

33. Zingg D, et al. The epigenetic modifier EZH2 controls melanoma growth and metastasis through silencing of distinct tumour suppressors. *Nat Commun*. 2015;6:6051.

34. Gao J, et al. Aberrant DNA methyltransferase expression in pancreatic ductal adenocarcinoma development and progression. *J Exp Clin Cancer Res*. 2013;32(1):86.

35. He S, et al. Potent Dual BET/HDAC Inhibitors for Efficient Treatment of Pancreatic Cancer. *Angew Chem Int Ed Engl*. 2020;59(8):3028–3032.

36. Benitz S, et al. Polycomb repressor complex 1 promotes gene silencing through H2AK119 mono-ubiquitination in acinar-to-ductal metaplasia and pancreatic cancer cells. *Oncotarget*. 2016;7(10):11424–11433.

37. Yoshida K, et al. Curcumin sensitizes pancreatic cancer cells to gemcitabine by attenuating PRC2 subunit EZH2, and the lncRNA PVT1 expression. *Carcinogenesis*. 2017;38(10):1036–1046.

38. Fazio EN, et al. Activating transcription factor 3 promotes loss of the acinar cell phenotype in response to cerulein-induced pancreatitis in mice. *Mol Biol Cell*. 2017;28(18):2347–2359.

39. Duan R, Du W, Guo W. EZH2: a novel target for cancer treatment. *J Hematol Oncol*. 2020;13(1):104.

40. Versemann L, et al. TP53-Status-Dependent Oncogenic EZH2 Activity in Pancreatic Cancer. *Cancers*. 2022;14(14):3451.

41. Kiryu S, et al. Prognostic value of immune factors in the tumor microenvironment of patients with pancreatic ductal adenocarcinoma. *BMC Cancer*. 2021;21(1):1197.

42. Yu M, et al. Prognostic value of tumor-associated macrophages in pancreatic cancer: a meta-

analysis. *Cancer Manag Res*. 2019;11:4041–4058.

43. Clark CE, et al. Dynamics of the immune reaction to pancreatic cancer from inception to invasion. *Cancer Res*. 2007;67(19):9518–9527.

44. Nutt SL, et al. EZH2 function in immune cell development. *Biol Chem*. 2020;401(8):933–943.

45. Shao F-F, Chen B-J, Wu G-Q. The functions of EZH2 in immune cells: Principles for novel immunotherapies. *J Leukoc Biol*. 2021;110(1):77–87.

46. Zhu Y, et al. Tissue-Resident Macrophages in Pancreatic Ductal Adenocarcinoma Originate from Embryonic Hematopoiesis and Promote Tumor Progression. *Immunity*. 2017;47(2):323-338.e6.

47. Saka D, et al. Mechanisms of T-Cell Exhaustion in Pancreatic Cancer. *Cancers (Basel)*. 2020;12(8):2274.

48. Delgiorno KE, et al. Identification and manipulation of biliary metaplasia in pancreatic tumors. *Gastroenterology*. 2014;146(1):233-244.e5.

49. Pin CL, et al. The bHLH transcription factor Mist1 is required to maintain exocrine pancreas cell organization and acinar cell identity. *J Cell Biol*. 2001;155(4):519–530.

50. Hesler RA, et al. TGF-β-induced stromal CYR61 promotes resistance to gemcitabine in pancreatic ductal adenocarcinoma through downregulation of the nucleoside transporters hENT1 and hCNT3. *Carcinogenesis*. 2016;37(11):1041–1051.

51. Karamitopoulou E. The Tumor Microenvironment of Pancreatic Cancer. *Cancers (Basel)*. 2020;12(10):E3076.

52. Wörmann SM, et al. Loss of P53 Function Activates JAK2-STAT3 Signaling to Promote Pancreatic Tumor Growth, Stroma Modification, and Gemcitabine Resistance in Mice and Is Associated With Patient Survival. *Gastroenterology*. 2016;151(1):180-193.e12.

53. Hessmann E, et al. Epigenetic treatment of pancreatic cancer: is there a therapeutic perspective on the horizon? *Gut*. 2017;66(1):168–179.

54. Hingorani SR, et al. Preinvasive and invasive ductal pancreatic cancer and its early detection in the mouse. *Cancer Cell*. 2003;4(6):437–450.

55. Tuveson DA, et al. Mist1-KrasG12D knock-in mice develop mixed differentiation metastatic exocrine pancreatic carcinoma and hepatocellular carcinoma. *Cancer Res*. 2006;66(1):242–247.

56. Choi E, et al. Expression of Activated Ras in Gastric Chief Cells of Mice Leads to the Full Spectrum of Metaplastic Lineage Transitions. *Gastroenterology*. 2016;150(4):918-930.e13.

57. Dobin A, et al. STAR: ultrafast universal RNA-seq aligner. *Bioinformatics*. 2013;29(1):15–21.

58. Liao Y, Smyth GK, Shi W. featureCounts: an efficient general purpose program for assigning sequence reads to genomic features. *Bioinformatics*. 2014;30(7):923–930.

59. McCarthy DJ, Chen Y, Smyth GK. Differential expression analysis of multifactor RNA-Seq experiments with respect to biological variation. *Nucleic Acids Res*. 2012;40(10):4288–4297.

60. Robinson MD, McCarthy DJ, Smyth GK. edgeR: a Bioconductor package for differential expression analysis of digital gene expression data. *Bioinformatics*. 2010;26(1):139–140.

61. Yu G, et al. clusterProfiler: an R package for comparing biological themes among gene clusters. *OMICS*. 2012;16(5):284–287.

62. Chen H, Boutros PC. VennDiagram: a package for the generation of highly-customizable Venn and Euler diagrams in R. *BMC Bioinformatics*. 2011;12(1):35.

63. Wu T, et al. clusterProfiler 4.0: A universal enrichment tool for interpreting omics data. *The Innovation*. 2021;2(3):100141.

64. Langmead B, Salzberg SL. Fast gapped-read alignment with Bowtie 2. *Nat Methods*. 2012;9(4):357–359.

65. Shen L, et al. ngs.plot: Quick mining and visualization of next-generation sequencing data by integrating genomic databases. *BMC Genomics*. 2014;15:284.

66. Ernst J, Kellis M. ChromHMM: automating chromatin-state discovery and characterization. *Nat Methods*. 2012;9(3):215–216.

67. Kowalik AS, et al. Mice lacking the transcription factor Mist1 exhibit an altered stress response and increased sensitivity to caerulein-induced pancreatitis. *Am J Physiol Gastrointest Liver Physiol*. 2007;292(4):G1123-1132.

68. Fazio EN, et al. Stanniocalcin 2 alters PERK signalling and reduces cellular injury during cerulein induced pancreatitis in mice. *BMC Cell Biol*. 2011;12:17.

69. Johnson CL, et al. Activation of Protein Kinase C delta leads to increased pancreatic acinar cell de-differentiation in the absence of MIST1. *J Pathol*. 2012;228(3):351–365.

70. Baker LA, Tuveson DA. Generation and Culture of Tumor and Metastatic Organoids from Murine Models of Pancreatic Ductal Adenocarcinoma. In: Su GH, ed. *Pancreatic Cancer*. New York, NY: Springer New York; 2019:117–133.

71. Huch M, et al. In vitro expansion of single Lgr5+ liver stem cells induced by Wnt-driven regeneration. *Nature*. 2013;494(7436):247–250.

72. Huch M, et al. Unlimited in vitro expansion of adult bi-potent pancreas progenitors through the Lgr5/R-spondin axis. *EMBO J*. 2013;32(20):2708–2721.

Figures Legends:

Figure 1. *KRAS^{G12D}* promotes increased K27me3 enrichment in pancreatic acini. (A) Representative images of H&E-stained pancreatic tissue from control and *KRAS^{G12D}* mice 22 days after TX gavage. Scale bar = 50 μm. **(B)** Heatmaps show K27me3 and K4me3 enrichment from 2 kb before the transcriptional start sites (TSS) to 2 kb after the transcriptional end site (TES) of all genes. Blue and yellow boxes indicate areas showing increased or decreased K27me3 enrichment in *KRAS^{G12D}* mice. There is reduced K27me3 at TSSs, which appears restricted in *KRAS^{G12D}* mice. **(C)** Comparison of called K27me3 and K4me3 enrichment at TSSs in control and *KRAS^{G12D}* acinar cells. Red dots represent genes with significantly dysregulated enrichment. Green line indicates expectation for equal enrichment between genotypes. **(D)** Comparison of chromatin states in control, *KRAS^{G12D}* and *KRAS^{G12D}EZH2$^{\Delta SET}$* mice 22 days after KRAS^{G12D} induction based on K4me3 and K27me3 enrichment. Numbers in first column indicate the percentage of each state across of the genome. Graphs show quantification of these numbers at the different gene regions. **(E)** Correlation between gene expression and chromatin states in control, *KRAS^{G12D}* and *KRAS^{G12D}EZH2$^{\Delta SET}$* pancreata 22 days after KRAS^{G12D} induction. Data represents the mean ± SEM (n=3 mice /group). Two-way ANOVA followed by Tukey's post hoc test was performed. In all cases, *P<0.05; **P<0.01; ***P<0.001.

Figure 2: Loss of EZH2 methyltransferase activity increases *KRAS^{G12D}*-mediated PanIN progression. Histological and quantitative analysis comparing *KRAS^{G12D}* and *KRAS^{G12D}Ezh2$^{\Delta SET}$* mice 51 days after initiating KRAS^{G12D} and 35 days after treatment with saline or cerulein. **(A)** Representative H&E images of pancreatic tissue. Boxplots indicate the amount of lesion area as a

percentage of the entire pancreatic tissue. Significance is measured by one-way ANOVA followed by Tukey's post hoc tests. **(B)** Representative IHC for CK19 or amylase followed by counterstaining with hematoxylin in cerulein-treated mice. Boxplots compare the ratio of $CK19^{+}$/$amylase^{+}$ tissue. Significance is measured by two-tailed unpaired Mann-Whitney test. Representative images of **(C)** alcian blue histology or **(D)** Periodic acid-Schiff (PSA) histology showing advanced lesions (arrows) in saline or cerulein-treated $KRAS^{G12D}$ and $KRAS^{G12D}Ezh2^{\Delta SET}$ mice. Boxplots compare the stained area as a percentage of ADM/PanIN lesions. Significance is measured by two-tailed unpaired Mann-Whitney test. In all cases, scale bar = 100 μm. For graphs, individual mice (n=7 mice per group) are shown and data represents the mean ± min to max. p value*≤0.05, **≤0.01. ns=not-significant.

Figure 3: Loss of EZH2 methyltransferase activity alters the effects of $KRAS^{G12}$ on expression of genes linked to the tissue microenvironment. (A) Volcano plot of RNA-Seq analysis between control and $KRAS^{G12D}$ pancreata 22 days after TX gavage. Significantly downregulated genes are shown in blue and significantly upregulated genes in red. Significance was evaluated with FDR≤0.05. **(B,C)** Similar Volcano plots comparing gene expression between $KRAS^{G12D}Ezh2^{\Delta SET}$ and **(B)** control or **(C)** $KRAS^{G12D}$ pancreatic tissue 22 days after activating $KRAS^{G12D}$ (n=3 mice). **(D)** KEGG pathway analysis performed on genes enriched for K27me3 and K4me3 identifies an increase in the state 4 pathways in $KRAS^{G12D}$ tissue (number of pathways) including unique enrichment of downstream mediators of KRAS signaling (red arrows). **(E)** KEGG pathway analysis based on DEGs from RNA-Seq identified enriched pathways between $KRAS^{G12D}$ (all pathways shown) or $KRAS^{G12D}EZH2^{\Delta SET}$ (top 20 pathways shown) and control tissue. Bars indicate -log10(p value) and dots indicate gene counts. Arrows indicate KRAS-related pathways unique

(red) or common (black) to each data set. **(F)** Gene Set Enrichment Analysis comparing enrichment of HALLMARK_KRAS_UP signalling between control, *KRAS*^{G12D} and *KRAS*^{G12D}*Ezh2*$^{\Delta SET}$ tissue 22 days following tamoxifen treatment. Normalized enrichment scores (NES) are significantly different between *KRAS*^{G12D}*Ezh2*$^{\Delta SET}$ and both control and *KRAS*^{G12D} expression (n=3).

Figure 4. EZH2 deletion alters immune cell infiltration promoted by KRAS^{G12D} after acute cerulein treatment. (A) KEGG pathway analysis of DEGs between *KRAS*^{G12D} and *KRAS*^{G12D}*Ezh2*$^{\Delta SET}$ pancreatic tissue 22 days after tamoxifen treatment. Bars indicate the FDR values while black dots indicate the number of genes associated with each pathway. **(B)** K27me3, K4me3 and RNA tracks showing bivalency and differential K27me3 enrichment between *KRAS*^{G12D} and control or *KRAS*^{G12D}*Ezh2*$^{\Delta SET}$ at *Cd1d2*. Red asterisks indicate K27me3 enrichment specific to *KRAS*^{G12D} mice. Tracks are an overlay of n=3 mice. **(C)** CD3, CD8, or F4/80 or **(D)** IF for CD4 positive cells in pancreatic tissue from *KRAS*^{G12D} and *KRAS*^{G12D}*Ezh2*$^{\Delta SET}$ mice 51 days after expressing KRAS^{G12D} and 35 days following cerulein treatment. Scale bar = 100 μm. Boxplots compare the mean number of positive cells and individual values (n=5 mice per condition) are included. Data are shown as mean ± min to max. Significance was measured using a two-tailed unpaired Mann-Whitney test. **p≤0.01. **(E)** Representative images of IHC for vimentin or α-SMA staining on pancreatic tissue. Scale bar = 100 μm.

Figure 5: Combined loss of MIST1 and EZH2$^{\Delta SET}$ promotes rapid loss of acinar tissue in the presence of *KRAS*^{G12D}. (A) RNA-seq analysis revealed marked increases in *Ezh2* in *Mist1*$^{creERT/-}$ *KRAS*^{G12D} pancreatic tissue 22 days after KRAS^{G12D} induction relative to all other genotypes and RNA tracks for *Ezh2* confirm deletion of exon 16 to 19 (red box). Data represents mean ± min to

max (n=3 for control, *Ezh2*$^{\Delta SET}$, *KRAS*^{G12D}, *KRAS*^{G12D}*Ezh2*$^{\Delta SET}$ and MKE and n=2 for *Mist1*$^{creERT/-}$*KRAS*^{G12D}). Letters indicate statistically similar groups. $p^b \leq 0.001$. **(B)** Representative western blots for EZH2, amylase or total ERK, 60 days after KRAS^{G12D} induction. RNA tracks for **(C)** *Ezh2* and **(D)** *Amy1*. Tracks are the overlay of n=3 mice. **(E)** Representative H&E-stained pancreatic sections 60 days after KRAS^{G12D} induction. Genotypes are indicated. Scale bar = 100 µm. **(F)** Boxplot quantifying the % lesion area in all genotypes based on H&E staining. Data is shown as mean ± min to max (n=4 for *Ezh2*$^{\Delta SET}$ and *KRAS*^{G12D}, n=6 for *Mist1*$^{creERT/-}$*KRAS*^{G12D}, n=7 for control, n=9 for *MKE* and n=14 for *KRAS*^{G12D}*Ezh2*$^{\Delta SET}$). Significance is measured by one-way ANOVA followed by a Tukey's post-hoc test. Different letters indicate statistically different p values; $p^b \leq 0.01$, $p^c \leq 0.001$. **(G)** Higher magnification images of H&E-stained pancreatic tissue from *MKE* mice. Green arrows indicate high grade PanIN lesions and putative PDAC that is only found in these animals. Scale bar= 50 µm.

Figure 6: *MKE* mice exhibit extensive ductal and PanIN lesion progression. *MKE* mice exhibit extensive ductal and PanIN lesion progression. Representative IHC for **(A)** amylase or **(B)** CK-19 on pancreatic tissue 60 days after KRAS^{G12D} induction. Genotypes are indicated. Scale bar = 100 µm. **(C)** Quantification of amylase staining in the various genotypes based on IHC staining. Data is shown as mean ± min to max (n=3 mice for *KRAS*^{G12D}, n=5 mice for *Ezh2*$^{\Delta SET}$, *KRAS*^{G12D}*Ezh2*$^{\Delta SET}$ and *Mist1*$^{creERT/-}$*KRAS*^{G12D}, and n=6 mice for control and *MKE*). Significance is measured by one-way ANOVA followed by a Tukey's post hoc test. $p^b \leq 0.001$. **(D)** Representative immunofluorescence for SOX9 on pancreatic sections 60 days after KRAS^{G12D} induction. Genotypes are indicated. Nuclei are counterstained with DAPI. White arrows identity positive SOX9 cells. Scale bar = 50 µm. **(E)** Quantification of SOX9 staining in the different mouse lines

based on IF staining. Data are shown as mean ± min to max (n=3 mice per conditions). Significance is measured by one-way ANOVA followed by a Tukey's post hoc test. Different letters indicate statistically different p values. $p^b \leq 0.001$, $p^c \leq 0.0001$.

Figure 7: Acinar-specific deletion of *Ezh2$^{\Delta SET}$* in *KRAS^{G12D}*-mediated PDAC alters the tumour microenvironment. **(A)** Representative H&E staining of pancreatic tissue from *Mist1$^{creERT/-}$KRAS^{G12D}* and *MKE* mice 22 days after KRAS^{G12D} induction. Green arrows indicate ADM. Scale bar = 50 µm. **(B)** Principal component analysis based on RNA-seq data 22 days after KRAS^{G12D} induction. **(C)** Volcano plot showing differentially expressed genes between *Mist1$^{creERT/-}$KRAS^{G12D}* and *MKE* mice 22 days after KRAS^{G12D} induction based on RNA-Seq. Genes with significantly lower or higher expression in *MKE* mice are indicated in blue and red, respectively. Significance was determined with a FDR ≤ 0.05. **(D)** Top 20 pathways identified by gene set enrichment analysis using GO terms based on RNA-seq ($p_{adj} \leq 0.05$). **(E)** Gene set enrichment analysis shows increased enrichment in KEGG pathways "Regulation of inflammation response" and "ECM organization in *MKE* tissue compared to *Mist1$^{creERT/-}$KRAS^{G12D}*. Similar analysis shows decreased enrichment of genes involved in "Nucleosome assembly" in *MKE* tissue. **(F)** Representative trichrome blue staining of pancreas section from control, *Ezh2$^{\Delta SET}$*, *KRAS^{G12D}*, *KRAS^{G12D}Ezh2$^{\Delta SET}$*, *Mist1$^{creERT/-}$KRAS^{G12D}*, and *MKE* mice 60 days after KRAS^{G12D} induction. Scale bar = 100 µm.

Figure 8: *EZH2$^{\Delta SET}$* deletion increases acinar-to duct cell metaplasia (ADM) in the absence of the tissue microenvironment. **(A)** Experimental design for acinar cell isolation and embedding into collagen 22 days after KRAS^{G12D} induction. **(B)** Representative images of cell clusters three and seven days after acinar cell isolation. Genotypes are indicated. Scale bar = 100 µm. **(C)**

Quantification of the percentage of cell clusters with visible ADM, one to nine days after acinar cell isolation. 50 or more clusters were counted for each condition. Data is shown as mean ± SEM (n=2 for *Mist1$^{creERT/-}$KRAS^{G12D}*, n=3 mice for *KRAS^{G12D}Ezh2$^{\Delta SET}$*, n=4 mice for *KRAS^{G12D}*, n=5 mice for *Ezh2$^{\Delta SET}$*, n=6 mice for control and n=7 mice for *MKE*). **(D)** Representative images of control acinar after seven days of treatment with increasing amounts of EZH2 inhibitor EPZ6438. Scale bar = 100 µm. **(E)** Quantification of 50+ acinar clusters for each condition. Data is shown as mean ± SEM. N=3. In all cases, significance was measured by a repeated measures ANOVA followed by Dunnett's correction. *p≤0.05, **p≤0.01, ***p<0.001.

Figure 9. *EZH2$^{\Delta SET}$* deletion has different cell autonomous roles depending on the context in which *KRAS^{G12D}* is expressed. (A) Morphology of *KRAS^{G12D}*, *KRAS^{G12D}Ezh2$^{\Delta SET}$* and *MKE* tissue two weeks after induction of CIP. Scale bar = 500 µm (left images), 100 µm (right images). **(B)** Representative images of organoids cultured in matrigel 1, 7 and 11 days after isolation. Cells were seeded at 5,000 cells. Genotypes are indicated. Scale bar = 2.4 mm. **(C)** Representative images of organoids 0, 5 and 7 days after first passage. Cells were seeded at 5,000 cells. Scale bar = 2.4 mm. **(D)** Quantification of organoid area 5 and 7 days after passage for *KRAS^{G12D}*, *KRAS^{G12D}Ezh2$^{\Delta SET}$* and *MKE* cultures. Data represents mean ± 95% CI. Number of organoids assessed is indicated above each data point. Significance is measured by two-way ANOVA followed by Tukey's correction. ***p≤0.001.

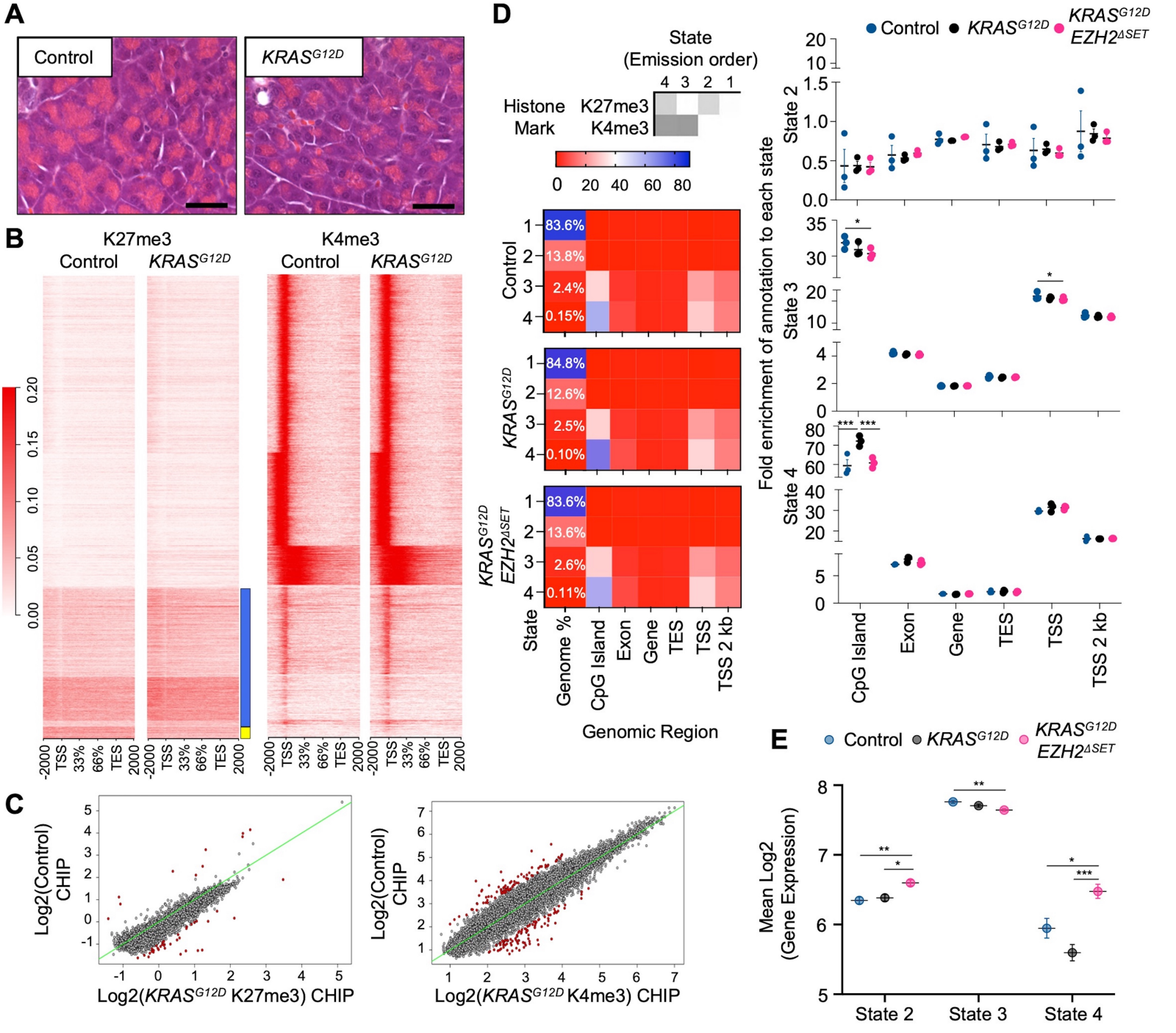
A
Control
KRASG12D
B
K27me3
Control
KRASG12D
K4me3
Control
KRASG12D
0.20
0.15
0.10
0.05
0.00
-2000
TSS
33%
66%
TES
2000
C
Log2(Control) CHIP
Log2(KRASG12D K27me3) CHIP
Log2(KRASG12D K4me3) CHIP
D
State (Emission order)
4 3 2 1
Histone Mark
K27me3
K4me3
0 20 40 60 80
Control
KRASG12D
KRASG12D EZH2ΔSET
83.6%
13.8%
2.4%
0.15%
84.8%
12.6%
2.5%
0.10%
83.6%
13.6%
2.6%
0.11%
State
Genome %
CpG Island
Exon
Gene
TES
TSS
TSS 2 kb
Genomic Region
Fold enrichment of annotation to each state
State 2
State 3
State 4
E
Control
KRASG12D
KRASG12D EZH2ΔSET
Mean Log2 (Gene Expression)
State 2
State 3
State 4

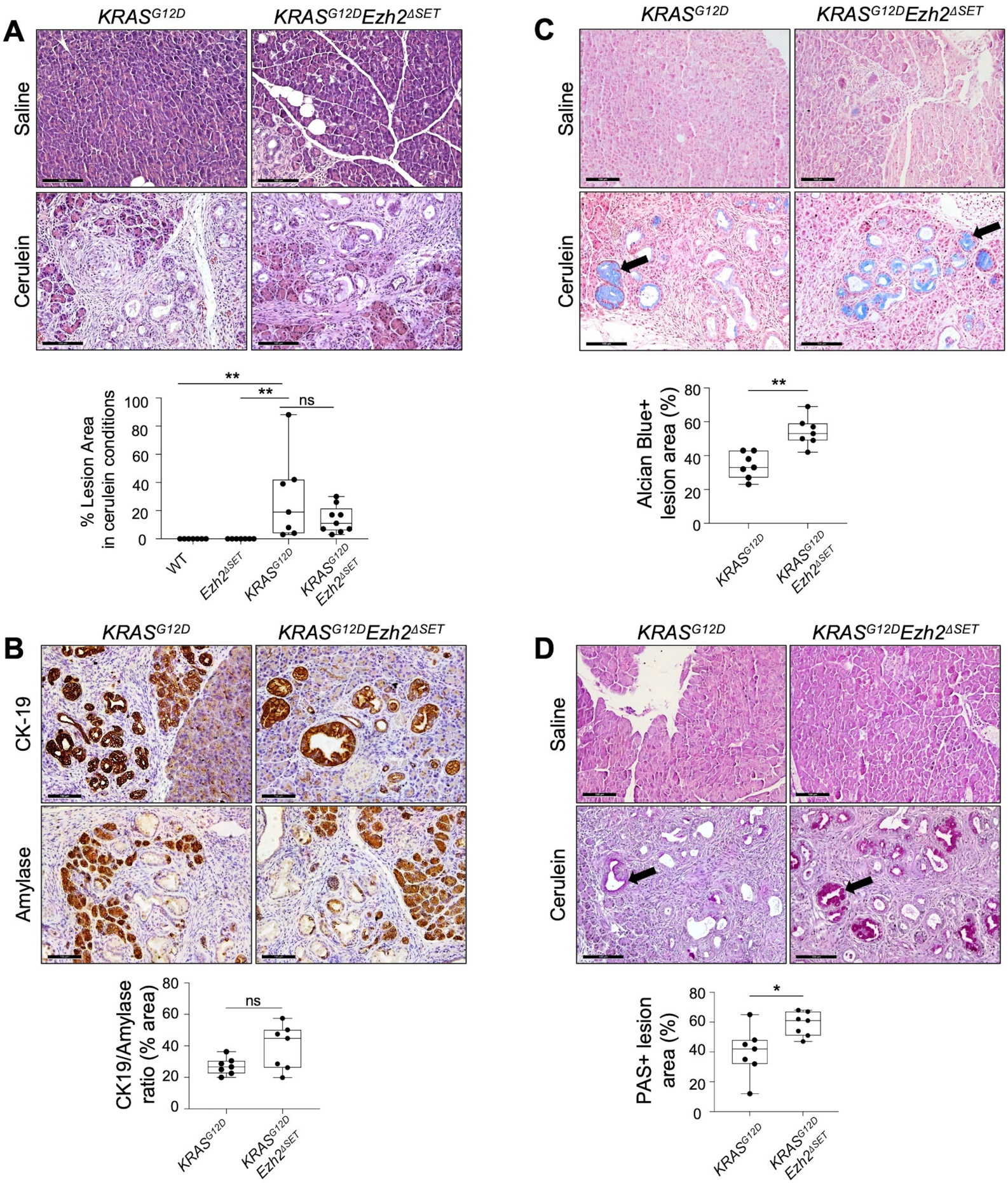
A
KRASG12D
KRASG12DEzh2ΔSET
Saline
Cerulein
% Lesion Area in cerulein conditions
**
**
ns
WT
Ezh2ΔSET
KRASG12D
KRASG12D Ezh2ΔSET
C
KRASG12D
KRASG12DEzh2ΔSET
Saline
Cerulein
Alcian Blue+ lesion area (%)
**
KRASG12D
KRASG12D Ezh2ΔSET
B
KRASG12D
KRASG12DEzh2ΔSET
CK-19
Amylase
CK19/Amylase ratio (% area)
ns
KRASG12D
KRASG12D Ezh2ΔSET
D
KRASG12D
KRASG12DEzh2ΔSET
Saline
Cerulein
PAS+ lesion area (%)
*
KRASG12D
KRASG12D Ezh2ΔSET

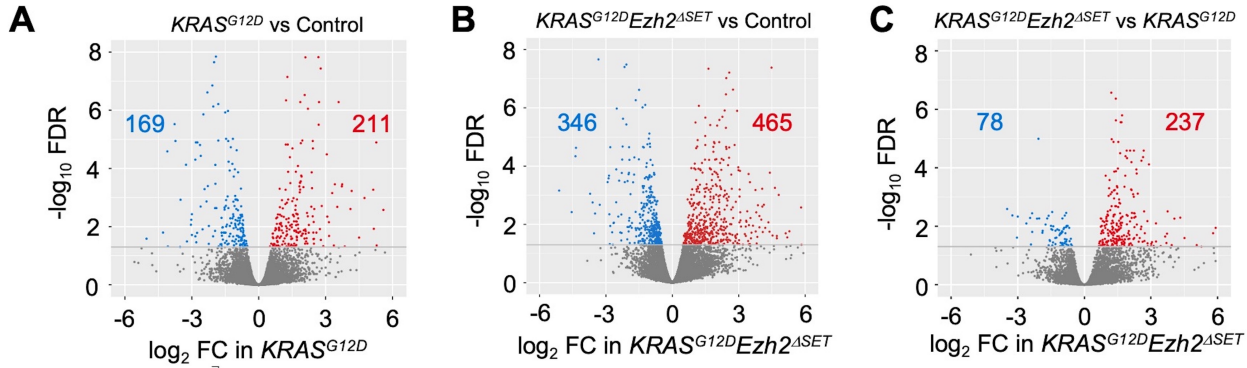
A
KRASG12D vs Control
169
211
-log10 FDR
log2 FC in KRASG12D
B
KRASG12DEzh2ΔSET vs Control
346
465
log2 FC in KRASG12DEzh2ΔSET
C
KRASG12DEzh2ΔSET vs KRASG12D
78
237
log2 FC in KRASG12DEzh2ΔSET

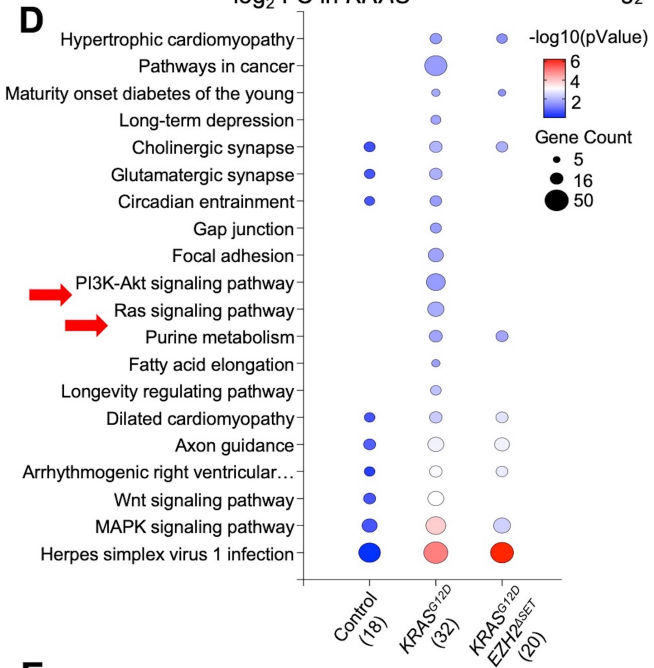
D
Hypertrophic cardiomyopathy
Pathways in cancer
Maturity onset diabetes of the young
Long-term depression
Cholinergic synapse
Glutamatergic synapse
Circadian entrainment
Gap junction
Focal adhesion
PI3K-Akt signaling pathway
Ras signaling pathway
Purine metabolism
Fatty acid elongation
Longevity regulating pathway
Dilated cardiomyopathy
Axon guidance
Arrhythmogenic right ventricular…
Wnt signaling pathway
MAPK signaling pathway
Herpes simplex virus 1 infection
-log10(pValue)
Gene Count
Control (18)
KRASG12D (32)
KRASG12D EZH2ΔSET (20)

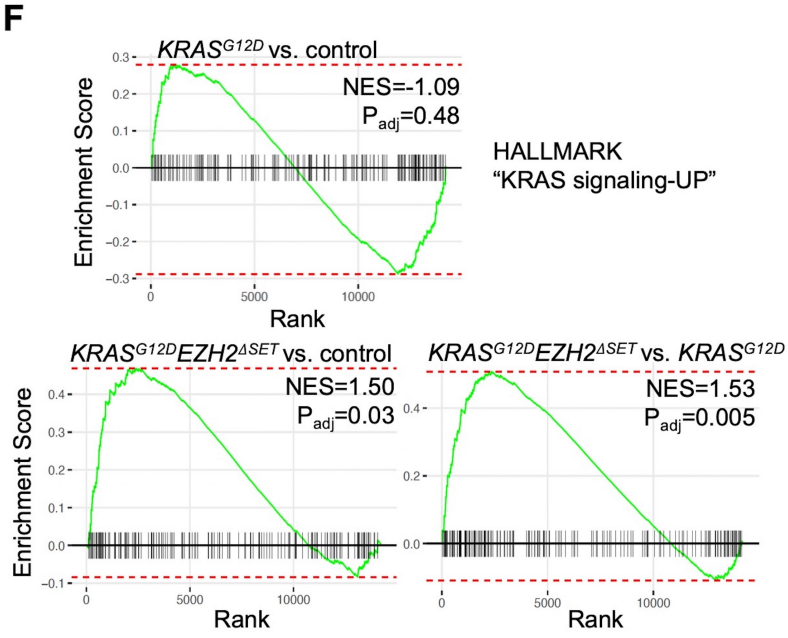
F
KRASG12D vs. control
NES=-1.09
Padj=0.48
HALLMARK
"KRAS signaling-UP"
Enrichment Score
Rank
KRASG12DEZH2ΔSET vs. control
NES=1.50
Padj=0.03
KRASG12DEZH2ΔSET vs. KRASG12D
NES=1.53
Padj=0.005

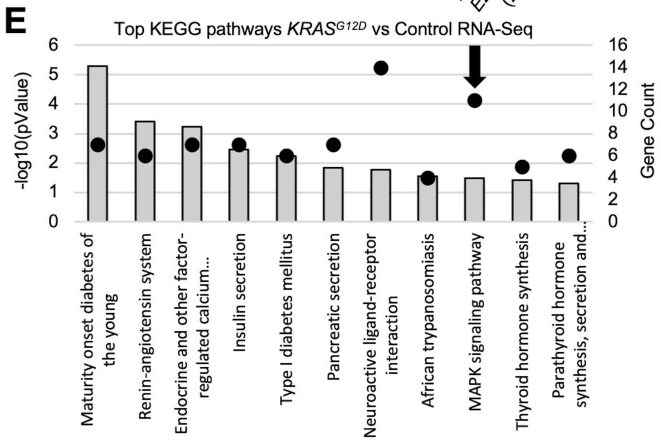
E
Top KEGG pathways KRASG12D vs Control RNA-Seq
-log10(pValue)
Gene Count
Maturity onset diabetes of the young
Renin-angiotensin system
Endocrine and other factor-regulated calcium…
Insulin secretion
Type I diabetes mellitus
Pancreatic secretion
Neuroactive ligand-receptor interaction
African trypanosomiasis
MAPK signaling pathway
Thyroid hormone synthesis
Parathyroid hormone synthesis, secretion and…

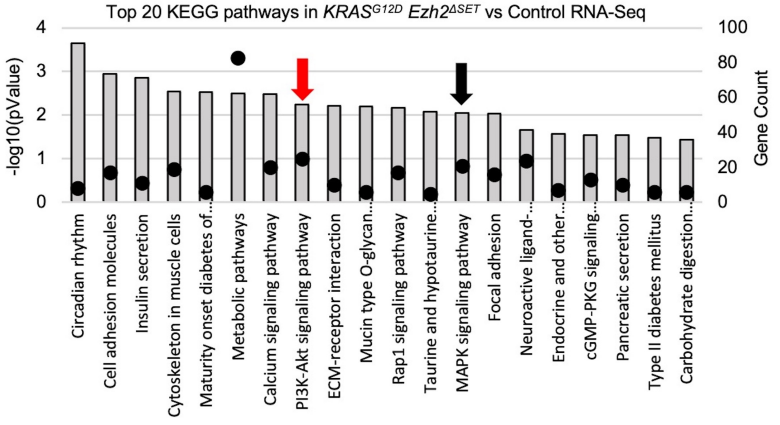
Top 20 KEGG pathways in KRASG12D Ezh2ΔSET vs Control RNA-Seq
-log10(pValue)
Gene Count
Circadian rhythm
Cell adhesion molecules
Insulin secretion
Cytoskeleton in muscle cells
Maturity onset diabetes of…
Metabolic pathways
Calcium signaling pathway
PI3K-Akt signaling pathway
ECM-receptor interaction
Mucin type O-glycan…
Rap1 signaling pathway
Taurine and hypotaurine…
MAPK signaling pathway
Focal adhesion
Neuroactive ligand-…
Endocrine and other…
cGMP-PKG signaling…
Pancreatic secretion
Type II diabetes mellitus
Carbohydrate digestion…

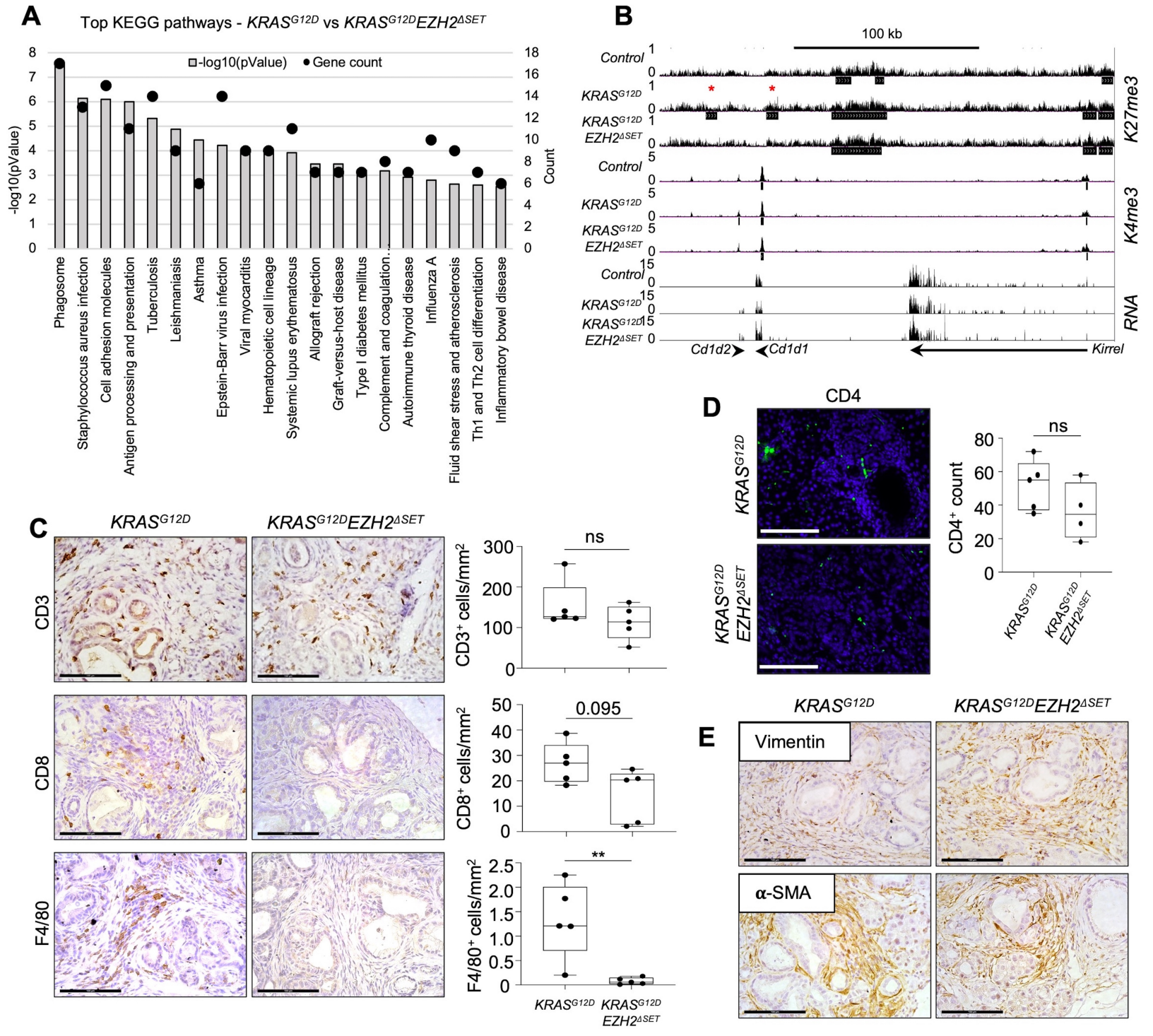
A
Top KEGG pathways - KRASG12D vs KRASG12DEZH2ΔSET
-log10(pValue)
Gene count
Count
Phagosome
Staphylococcus aureus infection
Cell adhesion molecules
Antigen processing and presentation
Tuberculosis
Leishmaniasis
Asthma
Epstein-Barr virus infection
Viral myocarditis
Hematopoietic cell lineage
Systemic lupus erythematosus
Allograft rejection
Graft-versus-host disease
Type I diabetes mellitus
Complement and coagulation...
Autoimmune thyroid disease
Influenza A
Fluid shear stress and atherosclerosis
Th1 and Th2 cell differentiation
Inflammatory bowel disease
B
100 kb
Control
KRASG12D
KRASG12D EZH2ΔSET
K27me3
K4me3
RNA
Cd1d2
Cd1d1
Kirrel
C
KRASG12D
KRASG12DEZH2ΔSET
CD3
CD8
F4/80
CD3+ cells/mm2
CD8+ cells/mm2
F4/80+ cells/mm2
ns
0.095
**
D
CD4
CD4+ count
E
Vimentin
α-SMA

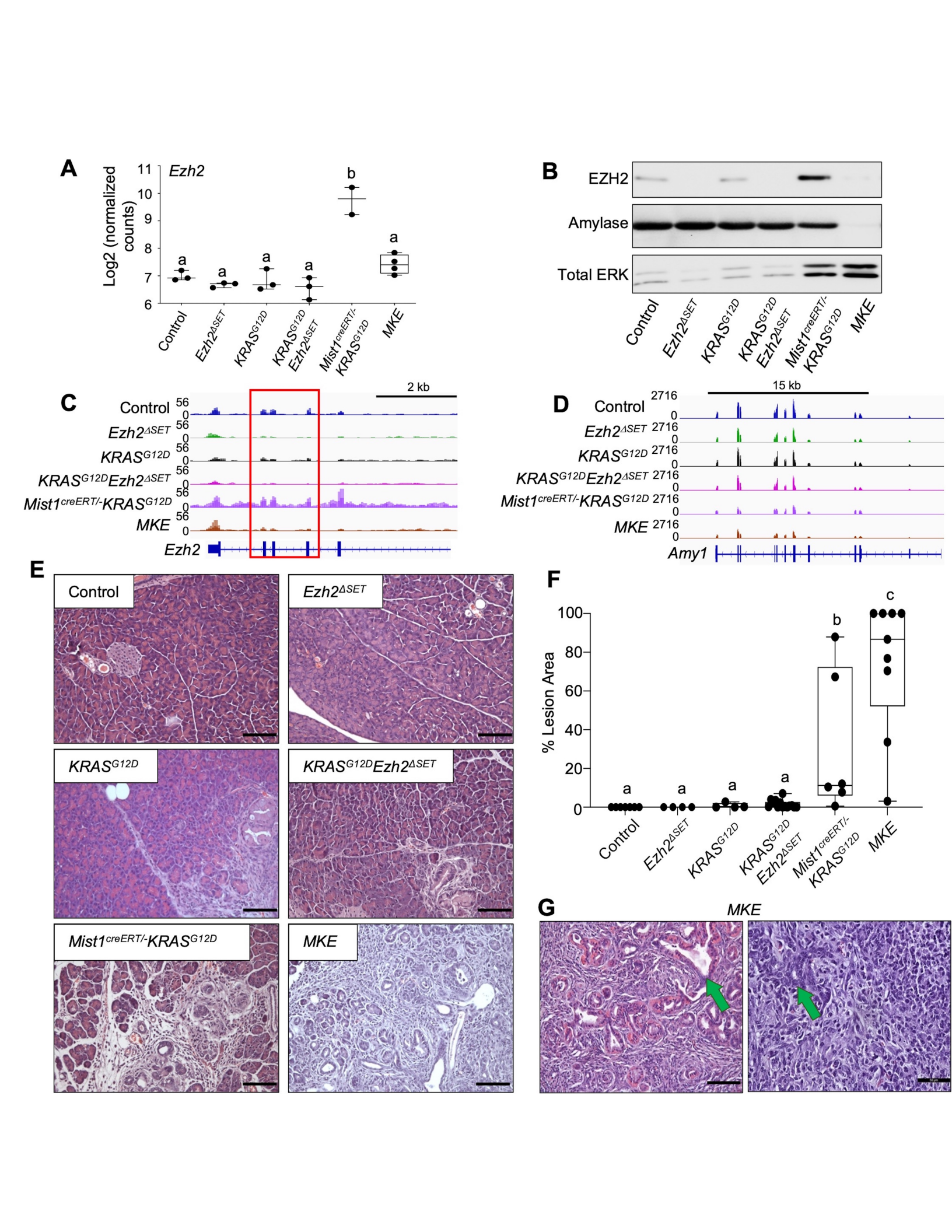
A
Ezh2
Log2 (normalized counts)
11
10
9
8
7
6
a
a
a
a
b
a
Control
Ezh2ΔSET
KRASG12D
KRASG12D Ezh2ΔSET
Mist1creERT/- KRASG12D
MKE
B
EZH2
Amylase
Total ERK
Control
Ezh2ΔSET
KRASG12D
KRASG12D Ezh2ΔSET
Mist1creERT/- KRASG12D
MKE
C
2 kb
Control
Ezh2ΔSET
KRASG12D
KRASG12D Ezh2ΔSET
Mist1creERT/- KRASG12D
MKE
Ezh2
56
0
D
15 kb
Control
Ezh2ΔSET
KRASG12D
KRASG12D Ezh2ΔSET
Mist1creERT/- KRASG12D
MKE
Amy1
2716
0
E
Control
Ezh2ΔSET
KRASG12D
KRASG12D Ezh2ΔSET
Mist1creERT/- KRASG12D
MKE
F
% Lesion Area
100
80
60
40
20
0
a
a
a
a
b
c
Control
Ezh2ΔSET
KRASG12D
KRASG12D Ezh2ΔSET
Mist1creERT/- KRASG12D
MKE
G
MKE

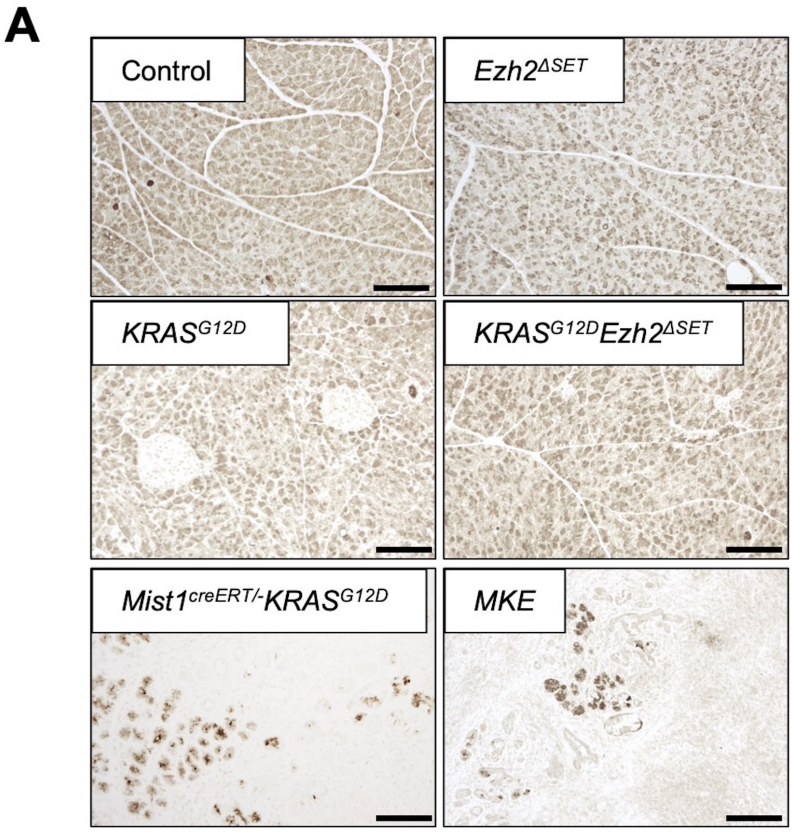
A
Control
Ezh2ΔSET
KRASG12D
KRASG12DEzh2ΔSET
Mist1creERT/-KRASG12D
MKE

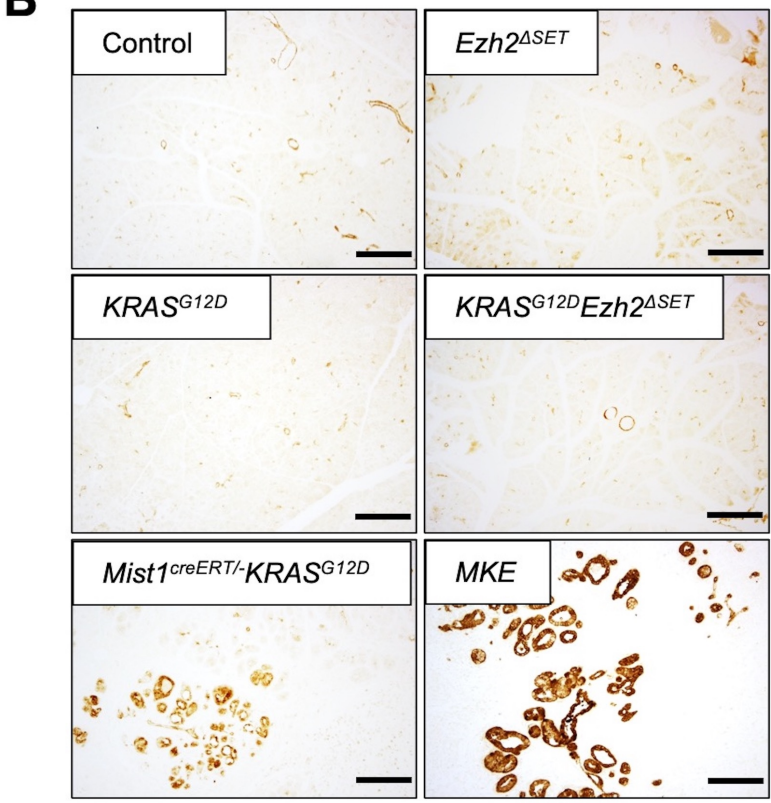
B
Control
Ezh2ΔSET
KRASG12D
KRASG12DEzh2ΔSET
Mist1creERT/-KRASG12D
MKE

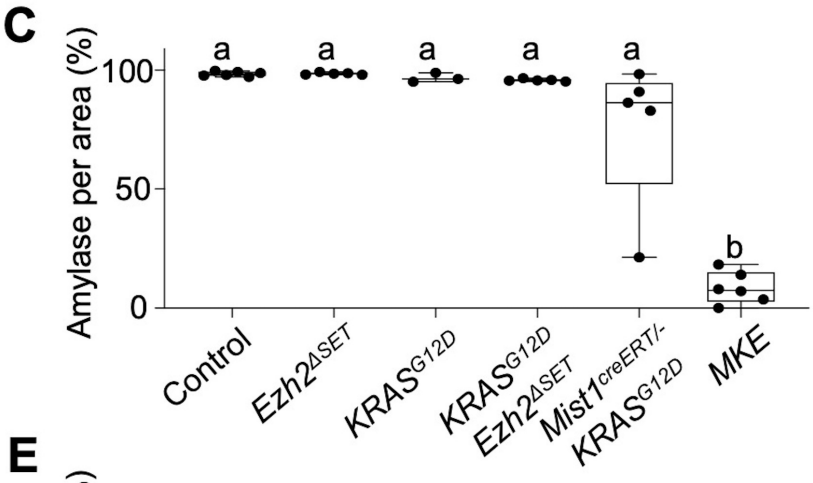
C
Amylase per area (%)
100
50
0
a
a
a
a
a
b
Control
Ezh2ΔSET
KRASG12D
KRASG12D Ezh2ΔSET
Mist1creERT/- KRASG12D
MKE

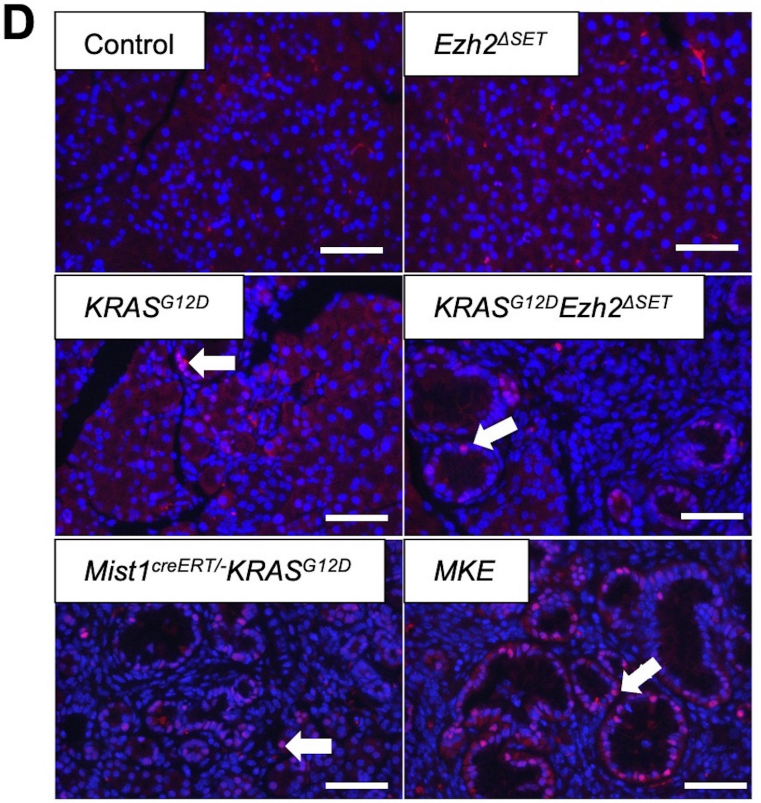
D
Control
Ezh2ΔSET
KRASG12D
KRASG12DEzh2ΔSET
Mist1creERT/-KRASG12D
MKE

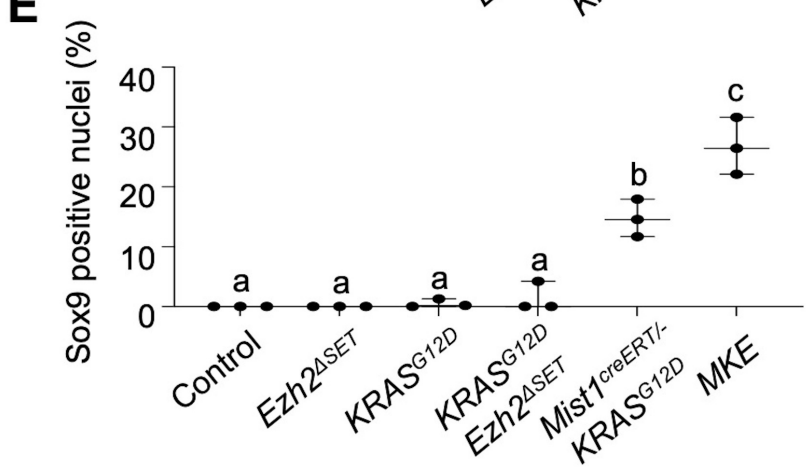
E
Sox9 positive nuclei (%)
40
30
20
10
0
a
a
a
a
b
c
Control
Ezh2ΔSET
KRASG12D
KRASG12D Ezh2ΔSET
Mist1creERT/- KRASG12D
MKE

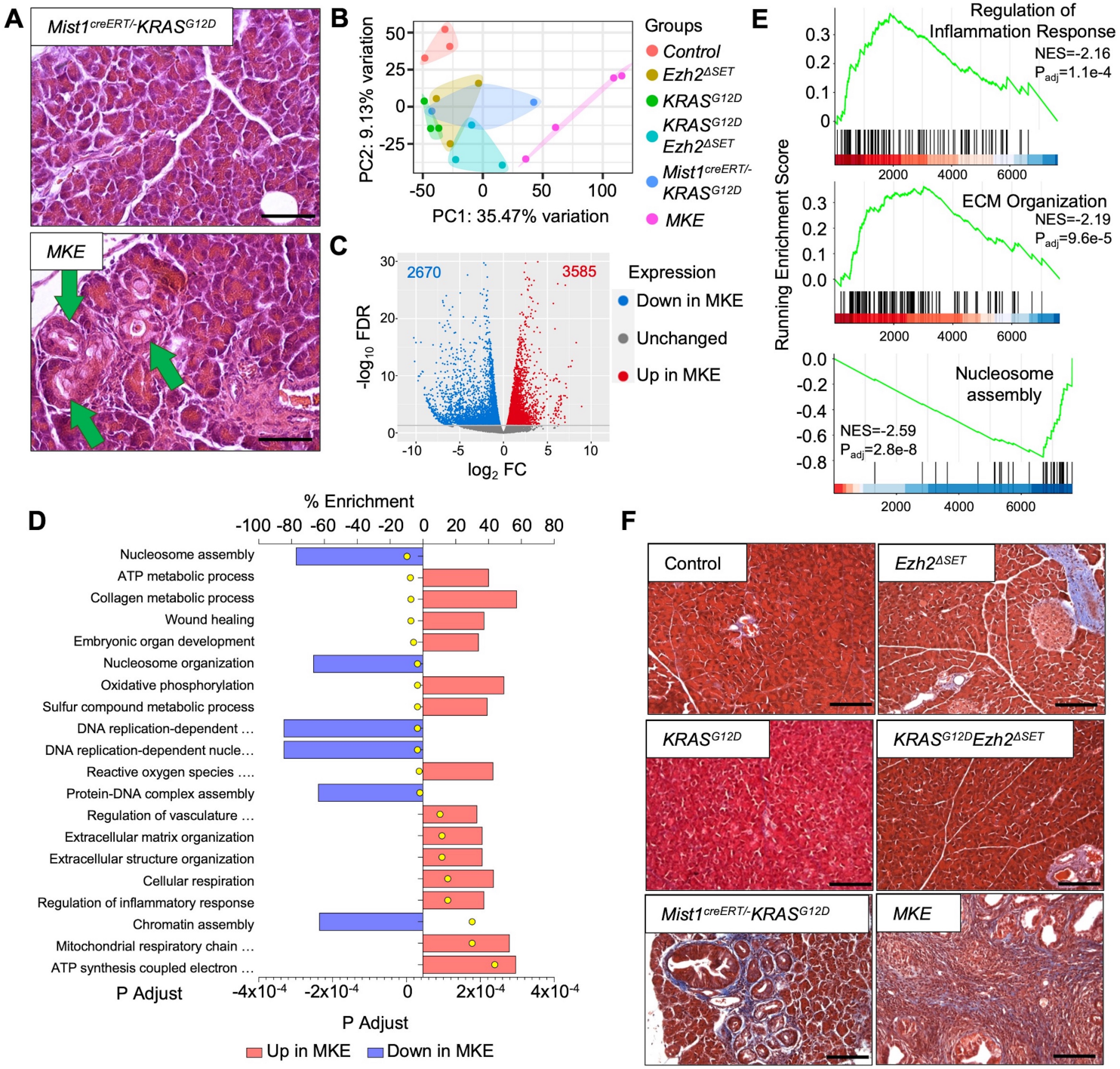
A
Mist1creERT/-KRASG12D
MKE
B
PC2: 9.13% variation
PC1: 35.47% variation
Groups
Control
Ezh2ΔSET
KRASG12D
KRASG12D Ezh2ΔSET
Mist1creERT/- KRASG12D
MKE
C
2670
3585
-log10 FDR
log2 FC
Expression
Down in MKE
Unchanged
Up in MKE
E
Regulation of Inflammation Response
NES=-2.16
Padj=1.1e-4
ECM Organization
NES=-2.19
Padj=9.6e-5
Nucleosome assembly
NES=-2.59
Padj=2.8e-8
Running Enrichment Score
D
% Enrichment
Nucleosome assembly
ATP metabolic process
Collagen metabolic process
Wound healing
Embryonic organ development
Nucleosome organization
Oxidative phosphorylation
Sulfur compound metabolic process
DNA replication-dependent …
DNA replication-dependent nucle…
Reactive oxygen species ….
Protein-DNA complex assembly
Regulation of vasculature …
Extracellular matrix organization
Extracellular structure organization
Cellular respiration
Regulation of inflammatory response
Chromatin assembly
Mitochondrial respiratory chain …
ATP synthesis coupled electron …
P Adjust
Up in MKE
Down in MKE
F
Control
Ezh2ΔSET
KRASG12D
KRASG12DEzh2ΔSET
Mist1creERT/-KRASG12D
MKE

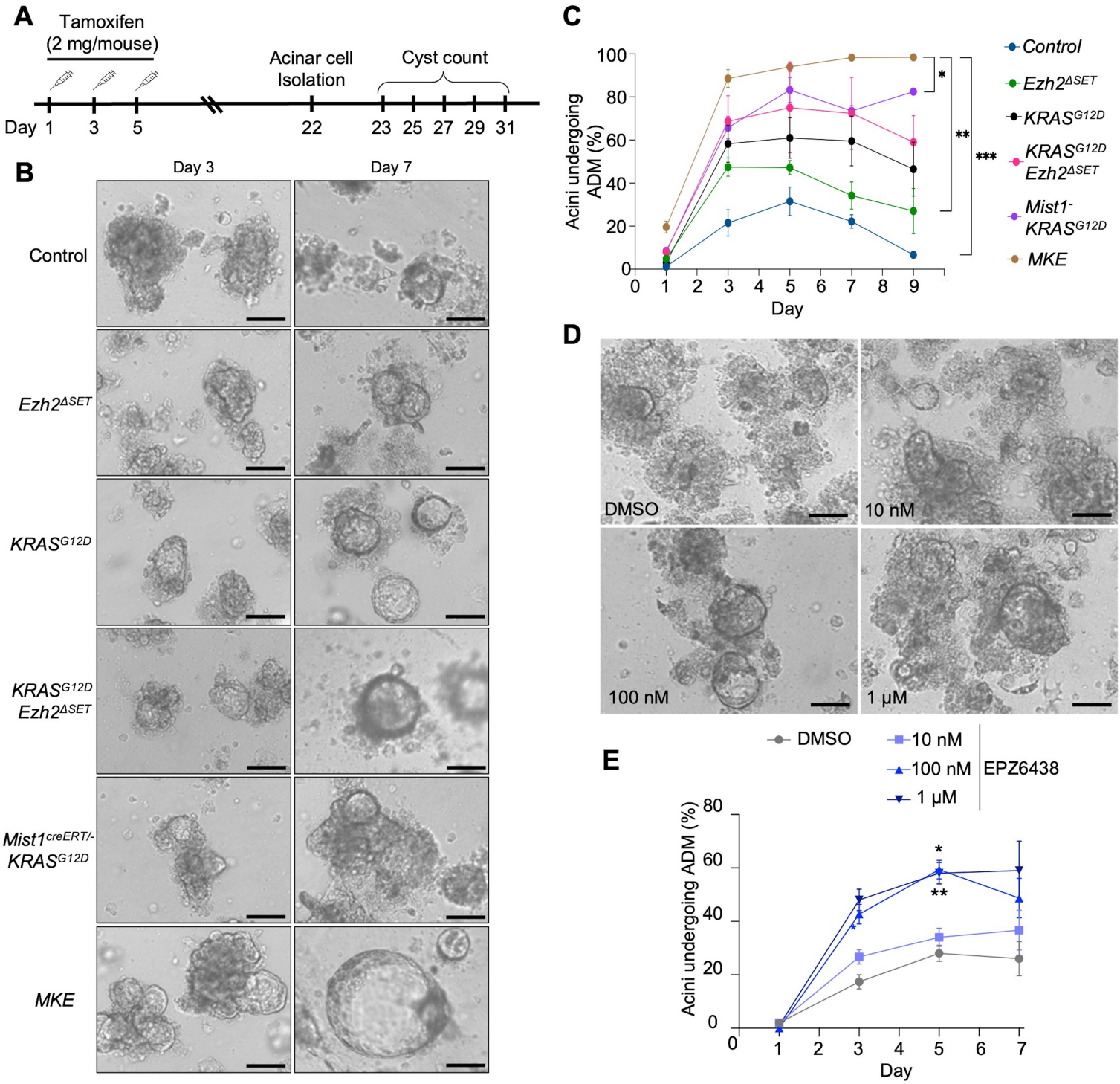
A
Tamoxifen
(2 mg/mouse)
Acinar cell
Isolation
Cyst count
Day 1 3 5 22 23 25 27 29 31
B
Day 3
Day 7
Control
Ezh2ΔSET
KRASG12D
KRASG12D
Ezh2ΔSET
Mist1creERT/-
KRASG12D
MKE
C
Acini undergoing
ADM (%)
Day
Control
Ezh2ΔSET
KRASG12D
KRASG12D
Ezh2ΔSET
Mist1-
KRASG12D
MKE
D
DMSO
10 nM
100 nM
1 μM
E
DMSO
10 nM
100 nM
1 μM
EPZ6438
Acini undergoing ADM (%)
Day

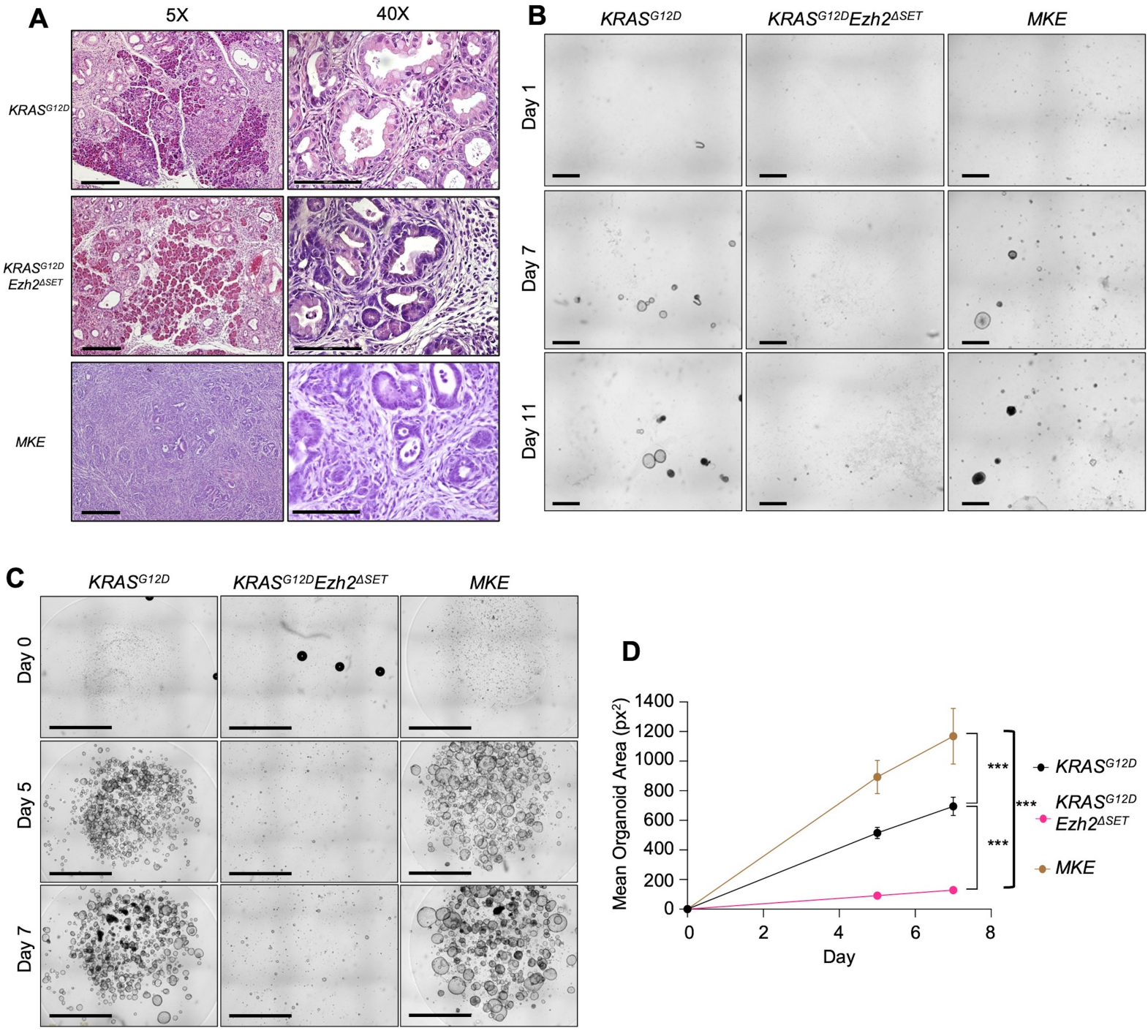
A
5X
40X
KRASG12D
KRASG12D Ezh2ΔSET
MKE
B
KRASG12D
KRASG12DEzh2ΔSET
MKE
Day 1
Day 7
Day 11
C
KRASG12D
KRASG12DEzh2ΔSET
MKE
Day 0
Day 5
Day 7
D
Mean Organoid Area (px2)
1400
1200
1000
800
600
400
200
0
0
2
4
6
8
Day
***
***
***
KRASG12D
KRASG12D Ezh2ΔSET
MKE